BRNO UNIVERSITY OF TECHNOLOGY

VYSOKÉ UČENÍ TECHNICKÉ V BRNĚ

FACULTY OF MECHANICAL ENGINEERING

FAKULTA STROJNÍHO INŽENÝRSTVÍ

INSTITUTE OF PHYSICAL ENGINEERING

ÚSTAV FYZIKÁLNÍHO INŽENÝRSTVÍ

CORRELATIVE TOMOGRAPHY

KORELATIVNÍ TOMOGRAFIE

MASTER'S THESIS
DIPLOMOVÁ PRÁCE

AUTHOR AUTOR PRÁCE	Bc. Karel Vařeka
SUPERVISOR VEDOUCÍ PRÁCE	Ing. Petr Bábor, Ph.D.

BRNO 2021

Assignment Master's Thesis

Institut:	Institute of Physical Engineering
Student:	**Bc. Karel Vařeka**
Degree programm:	Physical Engineering and Nanotechnology
Branch:	no specialisation
Supervisor:	**Ing. Petr Bábor, Ph.D.**
Academic year:	2020/21

As provided for by the Act No. 111/98 Coll. on higher education institutions and the BUT Study and Examination Regulations, the director of the Institute hereby assigns the following topic of Master's Thesis:

Correlative tomography

Brief Description:

The work will aim to measure and process 3D data structures from the semiconductor industry using correlative tomography. FIB–SIMS and SEM–EDX tomographic measurements will be combined with non–destructive X–ray tomography to show the possibilities of correlative tomographic analysis in identifying defects in structures from the semiconductor industry.

Master's Thesis goals:

1. Modify the current tomographic analysis procedure to perform automated measurements without the need to correct the imaging with a bismuth ion source for the TOF–SIMS5.
2. Perform a tomographic measurement on a selected sample from the semiconductor industry using the FIB–SIMS method.
3. Perform correlative analysis of 3D and 2D data of the selected sample by FIB–SIMS, NanoXCT, SEM, AFM, and EDX methods

Recommended bibliography:

BALIGA B. J.: Fundamentals of Power Semiconductor Devices, Springer, 2008

HEIDE, P.: Secondary ion mass spectrometry an introduction to principles and practices, John Wiley & Sons, Inc., 2014

CUI, Z.: Nanofabrication, Principles, Capabilities and Limits, Springer, 2008

REIMER, L.: Scanning Electron Microscopy, Physics of Image Formation and Microanalysis, Springer, 1998

Deadline for submission Master's Thesis is given by the Schedule of the Academic year 2020/21

In Brno,

L. S.

prof. RNDr. Tomáš Šikola, CSc. Director of the Institute	doc. Ing. Jaroslav Katolický, Ph.D. FME dean

ABSTRACT

The presented master's thesis deals with a correlative approach towards multiscale and multimodal analysis of through-silicon-via structures. The research is part of an international project concerning a failure characterization of said structures and implemented semiconductor devices. Correlative microscopy and tomography techniques of NanoXCT, FIB-SEM (EDS), FIB-SIMS, and AFM were proposed to establish a workflow of measurements. Focused ion beam tomography is a method of precise serial sectioning and obtaining valuable high-resolution images (FIB-SEM) or chemical composition maps (FIB-SIMS) at each cross-section. The following image registration shows the possibility of identifying defects as a function of structure depth. Additionally, the thesis outlines methods of image fusion of high-resolution and spectral images to most appropriately demonstrate the obtained data.

ABSTRAKT

Předložená diplomová práce se zabývá korelativním přístupem multimodální analýzy struktur prokovování s různým rozlišením. Výzkum je součástí mezinárodního projektu týkajícího se charakterizace poruch zmíněných struktur, které jsou implementovány v polovodičových zařízeních. Kombinace korelativní mikroskopie a tomografie technikami NanoXCT, FIB-SEM (EDS), FIB-SIMS a AFM byla navržena k zavedení opakovatelného pracovního postupu. Tomografie fokusovaným iontovým svazkem je metoda přesného odprašování v řezech, která mimo jiné v každém průřezu získává cenné snímky s vysokým rozlišením (FIB-SEM) nebo mapy chemického složení (FIB-SIMS). Následující transformace obrazu umožňuje identifikaci defektů jako funkci hloubky ve struktuře. Práce dále věnuje pozornost metodám sjednocení obrazů za účelem optimální prezentace získaných dat.

KEYWORDS

correlative microscopy, correlative tomography, FIB, SIMS, SEM, EDS, AFM, CT, image fusion, TSV

KLÍČOVÁ SLOVA

korelativní mikroskopie, korelativní tomografie, FIB, SIMS, SEM, EDS, AFM, CT, sjednocení obrazu, TSV

VAŘEKA, Karel. *Correlative tomography.* Brno, 2021. 70 p. Master's thesis. Brno University of Technology, Faculty of Mechanical Engineering, Institute of Physical Engineering. Supervised by Ing. Petr Bábor, Ph.D.

I hereby declare that I have written my master's thesis on the theme of *Correlative Tomography* independently, under the guidance of the master's thesis supervisor, Ing. Petr Bábor, Ph.D., and with the use of the technical literature and other sources of information which are all properly quoted in the thesis and detailed in the list of literature at the end of the thesis.

Bc. Karel Vařeka

Acknowledgement

At this point, I would like to thank my supervisor Ing. Petr Bábor, Ph.D., not only for his advice and comments during the laboratory experiments, but mostly for his guidance, friendly environment, and the opportunity to be a part of his team throughout my Bachelor's and Master's studies. I am thankful to Ing. Michal Potoček, Ph.D., for proofreading the thesis and pointing out ideas for measurements.

I am also thankful to Dr. Jürgen Gluch for his comments on the thesis and for supplementing his experimental data.

I am grateful to my friends who shared the university studies with me, cheered me up during the research work and in the last weeks of writing, and gave countless fond memories I will always remember.

Last but not least big thanks and sincere gratitude go to my family and my beloved girlfriend for always being there for me, for all the support, understanding, and additional feedback from a different point of view.

CzechNanoLab project LM2018110 funded by MEYS CR is gratefully acknowledged for the financial support of the measurements at CEITEC Nano Research Infrastructure.

This project is co-financed from the state budget by the Technology agency of the Czech Republic under the Epsilon Programme. The support is gratefully acknowledged.

Bc. Karel Vařeka

CONTENTS

Introduction **1**

1 Correlative tomography motivation **3**
- 1.1 Motivation . . . 3
- 1.2 Workflow . . . 4

2 Tomographic techniques **7**
- 2.1 X-Ray Computed Tomography . . . 7
  - 2.1.1 Experimental setup . . . 8
- 2.2 Focused Ion Beam . . . 9
  - 2.2.1 Liquid metal ion source . . . 9
    - Field evaporation . . . 10
  - 2.2.2 Ion beam column . . . 11
  - 2.2.3 FIB applications . . . 11
    - Scanning parameters . . . 12
- 2.3 Secondary Ion Mass Spectrometry . . . 14
  - 2.3.1 Ion-matter interaction . . . 14
    - Ion sputtering . . . 17
    - Matrix effect . . . 19
  - 2.3.2 Time-of-Flight mass spectrometer . . . 19
- 2.4 Scanning Electron Microscopy . . . 21
  - 2.4.1 Electron-matter interaction . . . 21
  - 2.4.2 Energy Dispersive X-ray Spectroscopy . . . 22

3 Through-Silicon-Via **25**
- 3.1 TSV fabrication . . . 26
  - 3.1.1 Etch process . . . 26
  - 3.1.2 Protection layer . . . 26
  - 3.1.3 Metallization . . . 26
- 3.2 TSV inspection . . . 27

4 2D and 3D measurements **29**
- 4.1 NanoXCT data . . . 29
- 4.2 FIB-SEM (EDS) . . . 32
  - 4.2.1 FIB serial sectioning . . . 32
  - 4.2.2 TSV sample preparation . . . 34
  - 4.2.3 Sample 9 FIB-SEM . . . 36
    - Cross-sectional EDS . . . 37
    - AFM topography . . . 38

FIB-SEM 3D tomography 39
4.3 FIB-SIMS 41
4.3.1 TOF-SIMS5 tomography geometry 41
4.3.2 SIMS rotary table adjustment 42
TOF-SIMS5 sample holder 42
Rotary table adjustment 42
Rotary table testing 44
4.3.3 Sample 9 FIB-SIMS 44
FIB-SIMS 3D tomography 47

5 Data correlation **49**
5.1 Image processing 49
5.1.1 Image filtering 49
5.1.2 Frequency domain 50
Curtaining removal 51
5.2 Image fusion 52
5.2.1 Intensity-Hue-Saturation fusion method 53
5.2.2 Pyramid based fusion 55

Conclusion **59**

References **61**

List of Abbreviations **69**

INTRODUCTION

Due to the need for miniaturization in the electrical industry, the demands on semiconductor devices are higher. This has led to the progress in the field of microscopy. These instruments handle the manufacturing, modification, and analysis of ever-shrinking semiconductor components. As techniques vary from multiple scales and resolutions, it is nowadays sometimes vague to perform the task of studying the specimen with only one instrument. Researchers are looking for ways to bring together different perspectives and merge insights from those techniques. Correlative microscopy (CM) combines diverse imaging and/or spectroscopy approaches, which offer different understandings of matter, chemical, and biological phenomena. Afterwards, for enhanced presentation of the results, the obtained information can be fused together.

The first correlative imaging occurred in the 1980s with the development of correlative light electron microscopy (CLEM). The earliest approach involved fluorescence light in combination with an electron microscopy signal. The immense contrast difference and localization ability allowed to view the same region of interest within the sample [1][1]. Since then, correlative microscopy has become more known to the scientific community. It has already yielded substantial support in the analysis of two-dimensional (2D) structures, primarily linking the viewing component with the chemical or biological context. This thesis follows up and improves the progress of correlative imaging and adds up the more challenging task of studying the underlying bulk using various tomographic techniques.

The word *tomography* is derived from the Greek word *"tomos"* meaning to slice/cut and *"graphō"* meaning to write/describe [2]. Tomography is a three-dimensional (3D) concept of structure evaluation. It is based on either penetrating an electromagnetic wave through the sample or, using a more recent concept, serial sectioning by focused ion beam (FIB) followed by imaging each slice. The aim of this thesis is to focus on performing and processing this type of analysis on structures and defects on and beneath the surface. Samples from the semiconductor industry are examined using CEITEC Nano facility instruments. Secondary ion mass spectrometry (SIMS), scanning electron microscopy (SEM), and chemical composition derived from energy-dispersive X-ray spectroscopy (EDS) were compared with non-destructive X-ray computed tomography (CT) and atomic force microscopy (AFM) data. First, the methods are to be modified to perform tomographic measurements, implemented into the presented workflow, and co-registered. Eventually, we carry out a comprehensive correlation of the results.

The thesis' structure is divided as follows: Chapter 1 further introduces the concept of correlative approach and outlines the executed workflow. In Chapter 2 the reader is introduced to the theoretical background of the instruments chosen for correlative measurements. Chapter 3 addresses the semiconductor sample of through-silicon-via adapted for correlative microscopy, its properties, and reasons for the study. The last two parts (Chapter 4 and Chapter 5) deal with the experimental realization of the actual measurement of samples and the following data processing and correlation.

---

[1] The text of the thesis works intensively with bibliography. For smoother reading and interaction with links to the literature sources, it is recommended to return to the original place in the text using the keyboard shortcut alt+left arrow.

1 CORRELATIVE TOMOGRAPHY MOTIVATION

Cool_PROMO is an international project connecting CEITEC Nano Research Infrastructure, Fraunhofer Institute for Ceramic Technologies and Systems IKTS, NenoVision, and many more. Its motto is "Process monitoring and failure analysis solutions for energy-efficient devices and products in microelectronics." Our task is to propose an experimental workflow, analyze, understand, present, and correlate the results of the required samples. Currently, the structures of through-silicon-via (TSV) studied in this thesis are developed and provided by a semiconductor company. For more information on TSV, see Chapter 3.

The following text deals with the correlative microscopy introduction, motivation, and workflow of TSV failure research using the methods and techniques described in chapter Chapter 2.

1.1 Motivation

Complementary characterization of a desired region of interest using a variety of techniques is termed as *correlative microscopy*. This approach combines multiple insides of the studied specimen. Research starts from lower magnification to observe larger areas and, for example, more easily localize material defects, to zoomed in investigation of the structures in detail. By including multimodal techniques and principles into the process, it is possible to connect and fill in any missing information. Correlation enables researchers to maximize the usefulness of the study and answer any questions regarding the specimen.

Nonetheless, a network of structures, such as porosity in minerals [3], blood vessels [4], fibres in composites [5], and finally semiconductors hide its important information well beneath the surface in three dimensions (3D). Secondly, the structures can be evolving in a certain direction. In the case of TSVs studied in this thesis, the dimensions are in the range of tens and hundreds of µm and the defects may vary throughout the whole device. In this respect, 3D microscopy techniques are introduced to identify fundamental issues during manufacturing and TSV testing, such as trench profile and barrier layer uniformity. Figure 1.1 shows different 3D microscopy techniques with respect to its resolution and the volume of the material that can be analyzed.

For the complexity of the TSV, we propose the correlative microscopy of cross-section followed by the correlative tomography of the underlying bulk. Non-destructive X-ray computed tomography, SEM high-resolution imaging, spectroscopy, and topography techniques were applied to the TSV to bridge a range of scales and provide useful and more comprehensive conclusion to the manufacturer. For better results, presentation and understanding, the outputs of these methods were combined via image fusion algorithms (Section 5.2). While conceptually the same, the process of registering larger structures hidden beneath the sample´s surface with the adoption of different methods are considerably more challenging.

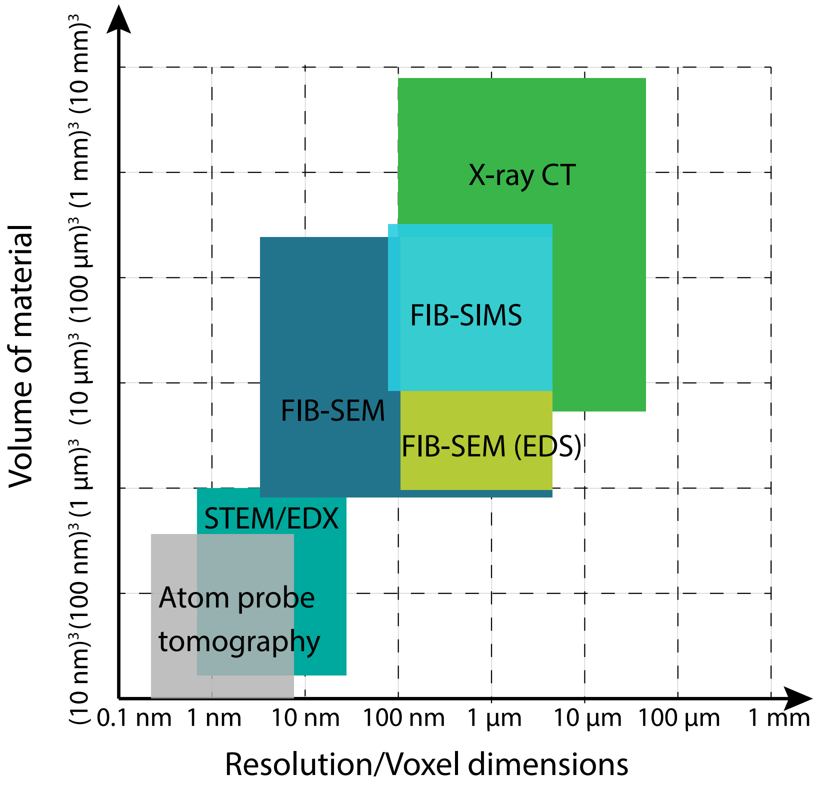

Figure 1.1: Comparison of FIB tomography techniques with other 3D microscopy methods with respect to resolution and analyzed area. Based on figures from [6, 7].

1.2 Workflow

As technological development moves forward, to keep up with these demands, semiconductor manufacturers try to come up with modern improvements. TSV is one of the technologies that has begun to come to the forefront of 3D integrated circuits in recent years. Of course, there are several complications during its development before a component is launched into mass production. Whether it is a complete malfunction or merely a decrease of the transferred signal caused in particular by a leakage current (Section 3.2).

Implemented TSVs within a silicon wafer are approximately 50 µm long in diameter and around 300 µm deep. The whole area is examined for irregularities of output characteristics by a probe station on-wafer system. This test detects a predefined electrical response on the conductor by placing two pins on the wafer at certain locations. In the case of CMOS[1] integreated TSV, capacitance fluctuations are measured and faulty regions are marked. Another technique is thermography signal variation. Correlations between thermography anomalies of in-wafer TSV and defect position have been ascertained.

---

[1] Complementary Metal Oxide Semiconductor.

Once the faulty areas are identified, the origin, cause, and prevention need to be found. The Cool_PROMO project connects institutions that are able to answer these questions. Firstly, the TSV proposed for further examination is cut out from the wafer by a diamond blade saw. During the cutting the wafer is cooled down with water and via a hot wax carrier plate transferred and glued on a steel cylinder-like base, as illustrated in Figure 1.2. This cylinder pillar serves as a holder for better handling between transportation and manipulation during X-ray tomography. Unfortunately, for SIMS and SEM analysis, this geometry is not very appropriate (more about that in Subsection 4.2.2). For comparison with the functional TSV, reference samples are also included and attached to the steel pin. As a result, it is possible to distinguish features that could cause the leakage current.

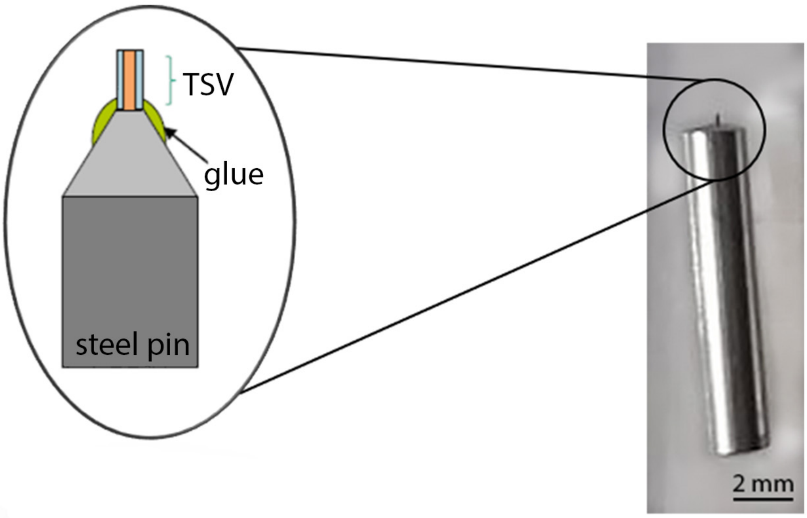

Figure 1.2: TSV sample mounted on top of the steel pin. Courtesy of Fraunhofer IKTS.

Presently, our workflow for the co-registration of successive techniques is applied at increasing magnifications to focus on the same submerged volume of interest. First, TSVs introduced to the follow-up investigation are moved to the Fraunhofer IKTS, where the lift out is executed. There, X-ray computed tomography is used to scan the entire TSV sample (Section 4.1). Based on the initial results, areas of TSV that may exhibit reasons of integrated circuit (IC) failure are selected and registered. The obtained tomography dataset is sent together with the samples to the CEITEC infrastructure, where author of this thesis continues with the experiments. Second, we reconstruct the processed NanoXCT slices in order to create a 3D model of the analyzed sample. The reconstruction serves as a beacon to find inconsistencies, thus confirm the area of interest and to outline the following procedure. As an example, we mention the possibility to model a cut position, depth, and an angle. Third, the actual section is performed by the focused ion beam according to the XCT 3D model slice (Section 4.2). Hence, the resulting area represents a cross-section of the TSV sample with all visible layers. This area is now ready for both surface and chemical analysis. Tools such as high-resolution SEM accompanied with EDS detector and TOF-SIMS were adapted for measurements. Both

EDS and TOF-SIMS provide a chemical composition study, however, the sensitivity can vary up to three orders of magnitude in favor of SIMS. EDS, on the other hand, is a non-destructive technique and can be obtained concurrently with secondary electron images in a relatively short time.

To distinguish any topographic irregularities of the cross-section, AFM measurement in collaboration with NenoVision company was performed. Finally, the tomographic procedures follow up using the above-mentioned methods to determine the development of defects through the sample. This thesis presents the proposal, measurements, and data evaluation of a representative TSV sample, marked by manufacturer as *sample 9*.

2 TOMOGRAPHIC TECHNIQUES

Tomography is a technique mediating the visualization of a specimen. The interest in 3D studies arises from the fact that bulk materials are generally opaque. Besides, considering the semiconductor industry, the relevant information is frequently hidden beneath the sample's surface. Moreover, since the electrical components are aiming towards shrinking its dimensions, to further improve density, power, and functionality, integrated circuits are beginning to stack into 3D assemblies. Thus, additional in-depth study requirements are emerging.

Historically speaking, tomography is a noninvasive quantitative sectioning of a bulk matter. It is based on the penetrating wave of various energies through the sample or the excitation of either an electric or a magnetic field. The first successful attempt to obtain tomographic images was carried out by Bartolomew and Casagrande in 1957 [8].

Yet, the word tomography has acquired another meaning as a result of development of nano-machining tools. Focused ion beam (FIB) is becoming more popular due to the unique capabilities it possesses. With the FIB implementation in a scanning electron microscope system called dual-beam FIB-SEM, it has become possible to precisely monitor the sample nanofabrication. One of the examples is high-precision sectioning and visualization of individual slices to generate 3D tomographic images [9]. Additionally, dual-beam systems can be supplied with a variety of detectors allowing for chemical (EDS), crystallographic (EBSD) or topographic (AFM) data to be obtained at each slice [10]. Alternatively, as a part of author's bachelor's thesis [11], the first tomographic measurement has been successfully performed with the newly installed FIB into the TOF-SIMS instrument in CEITEC laboratories. This upcoming chapter describes several techniques suitable for performing tomographic measurements.

2.1 X-Ray Computed Tomography

Computed tomography (CT) is a non-invasive technique of object visualization. Its main application is in the medical study and testing of manufactured components, i.e., detection of internal defects, as the sample dimensions in CT are very versatile. Voxel[1] size can differ from nm to cm scale [8].

The principle lies in the detection of high-energetic photons passing through the specimen. This transmission tomography delivers a reduced intensity of radiation after its interaction with the object. The beam intensity variation is described by the equation, known as the Beer-Lambert law [8]:

---

[1] Three-dimensional pixel representing information in a volume.

$$N_1 = N_0 \exp\left\{-\int \mu(x)\, dx\right\}. \tag{2.1}$$

The number of emitted photons N_0, resp., its intensity I_0 is known. Measuring the number of transmitted photons, resp., its intensity I_1, can determine the linear attenuation coefficient μ with respect to the slice thickness x. μ depends on the function of density and the atomic number. Mathematical algorithms (filtered back projection) and software (e.g., Fiji ImageJ [12] and Xradia XMRecontructor [13]) are then used to recreate a cross-sectional images and the following 3D volumetric data reconstruction.

2.1.1 Experimental setup

The CT setup configurations differ according to the application. The prominent system for the industrial field (see Figure 2.1) consists of a stable source of X-rays, a rotational sample under investigation, and a detector. As the sample rotates, X-ray projections in different directions can be collected and processed.

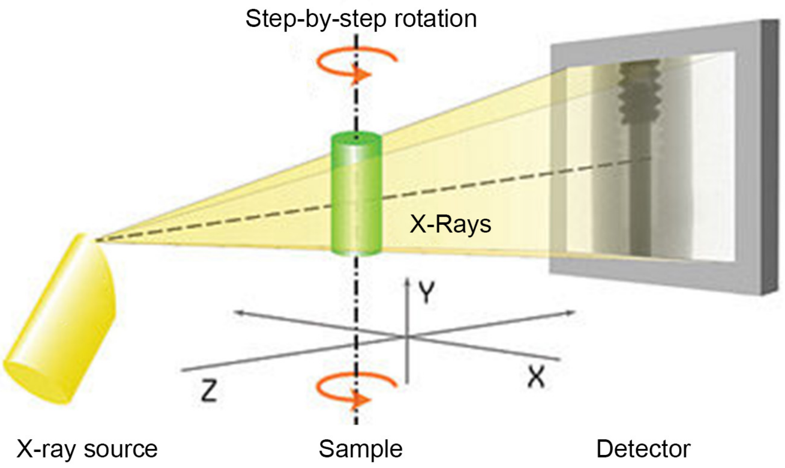

Figure 2.1: The basic principle of CT setup with cone beam geometry and rotational sample stage. Adapted from [2].

X-rays are generated by charged particle acceleration or by atomic shell transition (Subsection 2.4.2). In the case of CT, electrons are accelerated by a potential difference of 10–100keV [2]. Upon striking the target (metal such as Cu, Mo or W), characteristic X-rays are produced. This radiation is coherent and has a narrow energy range. However, only a small fraction of the electron energy is transferred to the X-radiation, the rest being heat, secondary electrons and continuous spectrum [14]. Depending on the sample's chemical composition, the acceleration voltage needs to be adjusted to match the transmission parameters.

As a detector in CT instruments, *scintillator* is widely embraced. Transmitted photons interact with the scintillator material to produce visible light. The light continues to the set of photodiodes, where the current is generated via the photoelectric effect. The output signal is recorded by a transistor matrix, saving the relative coordinate position, and transferred into the digital form [8, 14]. What follows is a reconstruction of the measured data to create a slice image, which is beyond the scope of this work.

2.2 Focused Ion Beam

This section discusses the nano-machining tool adapted for the creation, modification, and deposition of nano structures. Popularity of focused ion beam has grown rapidly over the years in many science fields due to its unique properties and multiple complementary signals that can be collected. The principle is in a highly focused beam of ions incoming to a sample surface, which, by virtue of ion optics, results in low angular resolution, typically in hundreds and tens of nm. FIB devices differ in the extraction method and type of ions, current magnitude, etc. The most common one is the liquid metal source, which has also been used for the tomographic measurements performed in this thesis.

2.2.1 Liquid metal ion source

Liquid metal ion source (LMIS), also known as Liquid metal ion gun (LMIG[2]), or electrohydrodynamic ion source (by its extraction mechanism), is a field emission type of source commonly generating ions such as Ga^{+}, In^{+}, $\mathrm{Au_n}^{+}$, $\mathrm{Bi_n}^{q+}$ [15]. For example gallium is widely used for its unique properties, in particular low melting point and relative unreactivity[3]. Lower melting point (29.8° for Ga [16]) guarantees lower operating temperature and minimization of the adapted metal interdiffusion to and from the tip of the source.

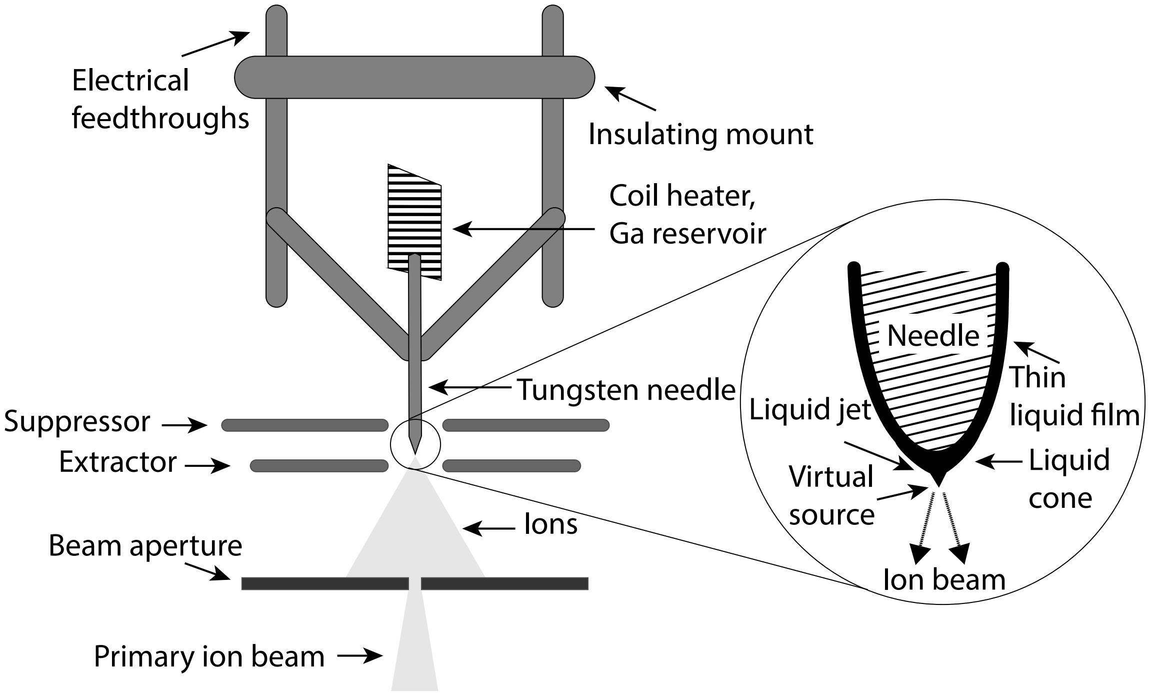
Electrical
feedthroughs
Insulating mount
Coil heater,
Ga reservoir
Tungsten needle
Suppressor
Extractor
Ions
Beam aperture
Primary ion beam
Needle
Thin
liquid film
Liquid jet
Liquid
cone
Virtual
source
Ion beam

Figure 2.2: A diagram of commercial liquid metal ion source found in FIB systems. This type of source has a lifetime of about 1500 µA h. Based on figure from [17].

LMIS consists of a tungsten cylinder-like needle with the tip in units of micrometers. The metal of interest (gallium) is stored in a reservoir. The emitter is heated to the melting point of the metal source to liquefy. During the heating process, the liquid metal is drawn out along the rod by external electrostatic and surface tension forces. The tip is now supplied with a thin film layer. This state can last a few weeks until eventually the gallium is depleted and a new heating is necessary. Applying the emission current to the needle, the apex is adjusted to a tip of radius ~1–2 nm [17]. This is referred to as *Taylor cone*, after British physicist and mathematician Geoffrey I. Taylor, who provided the mathematical description of the phenomenon in 1964 [6]. This conical shape is the result of an electric field stress balanced by the liquid surface tension force [18]. Figure 2.2 shows a sketch of LMIS.

---

[2] As the SIMS community refers it to.

[3] It has no significant effect on the secondary ion yield.

Once the hump is sharp enough, the external electric field causes ionization and extraction of gallium atoms. This field is created by a potential difference between the tip and a spherical electrostatic electrode called the extractor, charged in units of kiloelectron volts. Another electrode is a suppressor. The suppressor is maintained at the voltage of ≈2 kV. This keeps the ion beam current steady and limits undesirable ion emission from sides of the apex [17, 19].

Field evaporation

Field evaporation (FEV) is the field-induced removal of an atom from its lattice. Very strong external field distorts the atomic potential. The probability of electron tunneling increases, hence creating an ion, which eventually evaporates [18, 20]. Note that the ionization process can also occur after the atom evaporation from the lattice.

The field evaporation is a complicated phenomenon due to the strong space-charge effects near the emitter and the constant flow of liquid metal. To simplify, the activation energy Q_0 needed to produce an ion in free space is given by the equation [17]

$$Q_0 = \Lambda_0 + I_n - n\phi, \tag{2.2}$$

where Λ_0 represents surface binding energy, I_n refers to the ionization energy of n-atoms, and ϕ is the relevant local work function of the surface left after an atom removal. Richard Forbes in his paper [20] and book [21] continued with the Erwin Müller's evaporation field formula (1951) and presented this conclusion of the energy required for evaporation:

$$Q_E = \Lambda_E + I_n - n\phi - neEx - n^2e^2/16\pi\epsilon_0 x. \tag{2.3}$$

E denotes external field, Λ_E is binding energy in the field presence, e is the elementary charge and x is the distance of the nucleus from the electric surface.

In the evaporation field, the activation energy is zero. So-called electrostatic and image-potential terms evaluated at a certain distance x, have to be equal to one "thermodynamic" term, containing the binding energy, ionization and work function [22, 23]. By comparing these two statements and some additional assumptions [20], we get the Müller's escape field (otherwise known as *image-hump* mechanism) required for field evaporation at the top of the hump

$$E = \frac{4\pi\epsilon_0}{n^3e^3}\left[\Lambda_E + I_n - n\phi\right]^2. \tag{2.4}$$

This equation gives a certain estimate for the lowest external field required. It has been measured in [17] that the critical distance from the tungsten needle tip required for ion creation in the field of ∼10 V/nm is ∼0.2 nm. What is more, in reality, the inclusion of repulsive energy has to be taken into account.

2.2.2 Ion beam column

Once the ions are extracted, the importance lies in their properties. LMIS, in particular with gallium ions, is widely used for a variety of reasons [6, 18]:

- High source current density $\sim 10^6\,\mathrm{Acm^{-2}}$, up to 60 nA probe current.
- High brightness, for gallium this value is $1 \times 10^6\ \mathrm{Am^{-2}sr^{-1}V^{-1}}$.
- Geometry of LMIS reduces the spherical and chromatic aberrations ($\Delta E = 5\mathrm{eV}$), although adjustments by octupoles are required.
- Magnification up to 1000000×.
- Lower penetration volume (∼60 nm for gallium).

The beam of charged ions continues through a set of lenses and apertures to be focused to the desired spot size, as well as to modify the aberrations (consider Figure 2.3). The simplest and widely used architecture within the ion tubus is a set of two main lenses, i.e., the condenser and the objective [24]. Other optics are used for ion beam raster over the sample surface (deflection plates). To control the probe current[4], a set of selection apertures is included. Another way is the adjustment of condenser lenses. By applying a less positive voltage to the middle lens, the beam is more spread.

An octupole stigmator establishes a circular (Gaussian) beam profile. A beam blanker is added to deflect the continuous beam for precise exposition. A mass filter is occasionally included if the reservoir consists of a compound of two elements. This is the case of TOF-SIMS (Section 2.3), where Bi is separated from BiMn in the LMIG column. The whole tubus is held under vacuum of 10^{-6} Pa for proper operation and long lifetime.

Ions are almost exclusively focused via a set of electrostatic lenses, because, in contrast to electrons, require stronger fields due to its higher momentum. Because force $\mathbf{F} = q\mathbf{E}$ caused by an electric field is independent of the ion's velocity, whereas magnetic force $\mathbf{F_B} = q\mathbf{v} \times \mathbf{B}$ is not. Electrostatic lenses change ion's velocity. As a result slower moving ions are accelerated to reach the crossover spot simultaneously and vice versa. Magnetic optics call for very high currents, therefore the setup would be impractically large (10^3 kg) [17].

2.2.3 FIB applications

Focused ion beam is a versatile tool for many applications of industry. Its main advantage are µm and nm capabilities. Apparatus FIB-SEM allows users to observe the nanomachining of specimens. The sample material is possible not only to directly etch

---

[4] Probe current determines the amount of ions incoming to the sample.

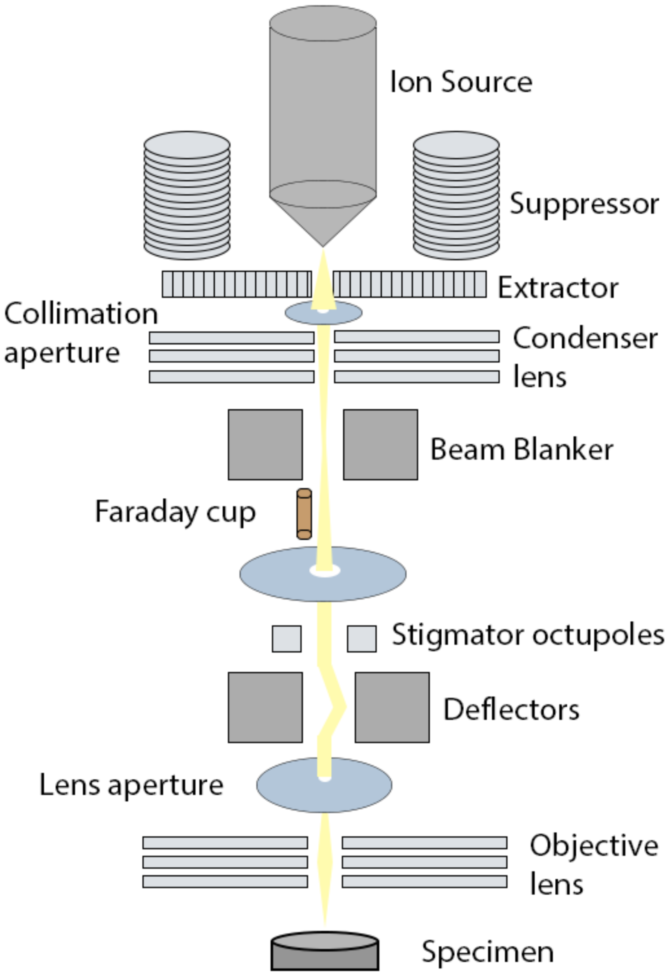
Ion Source
Suppressor
Extractor
Collimation aperture
Condenser lens
Beam Blanker
Faraday cup
Stigmator octupoles
Deflectors
Lens aperture
Objective lens
Specimen

Figure 2.3: Illustration of the major FIB column components. Drawing is not to scale. Based on figures from [16, 25].

or to mill bitmaps, but also deposit layers by a focused ion beam induced deposition process (FIBID) [16]. This is used specifically during lamella creation. The local deposition protects the lamella and assists during lift out and final placement on a TEM grid. However, deposition can be destructive to the outermost monolayers. Ions during the start of FIBID can sputter away these atoms. To prevent this, electron beam-induced deposition is firstly initiated to protect unwanted ion sputtering.

Simultaneously, as described in Subsection 2.3.1 and visualized in Figure 2.5, one of the ion-matter interaction products are *secondary electrons* (SE). By their detection, it is possible to image the topography with better surface sensitivity compared to the electron beam on account of the smaller interaction volume. Foremost, ion-induced secondary electrons display better contrast, as the ion interaction is more sensitive to an atomic number, nonetheless they do not reach the overall resolution of electron imaging.

Scanning parameters

As the impinging ions interact with the sample, unwanted events can arise and affect the overall quality of FIB processes. Parameters defining the primary ion beam, i.e., accelerating voltage, beam current, beam shape, and scanning parameters, have a great impact on the precision and the milling rate [26]. Pixel *dwell time* describes the time of a continuous ion beam in one spot. The way of ion beam progress between each pixel is called *scan direction* [6].

Layer by layer method creates parallel floor and is vastly used for imaging. Each beam pass sputters away a certain amount of material until the target depth is reached. This method is shown in Figure 2.4a. *Line by line* is serial milling. It guarantees a fast removal of large volumes because of its v-shaped crater and *edge effect*[5]. Applications are in cross section, polishing and thinning. This direction is sometimes prone to redeposition on the crater floor and sides (Figure 2.4b). During tomography sample preparation (Subsection 4.2.1), cross-section is often created by layer etching. The perpendicular area and the actual ROI sectioning are polished by line method [27].

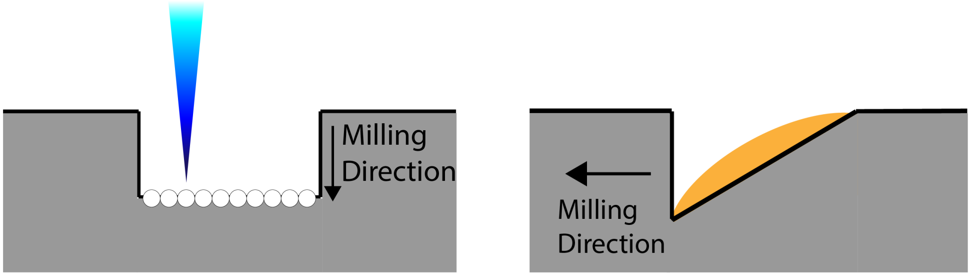

(a) Layer by layer.

(b) Line by line.

Figure 2.4: FIB scanning direction. (a) shows parallel sputtering with 0% pixel overlap as illustrated with non-overlapping circles. (b) etch in the serial direction to the cross-section. The yellow hump symbolizes occuring redeposition. Based on figure from [27].

---

[5] The sputter yield (Equation 2.14a) of atoms and molecules is increased at the protrusion or the edge of a step on a specimen surface.

2.3 Secondary Ion Mass Spectrometry

The fundamentals of SIMS were discovered in the first half of the 20th century by J. J. Thomson, when he confirmed the secondary ion presence. Since then, throughout the century, this method has gained great applications in the semiconductor and photoelectric industry. Nowadays, SIMS is especially aimed at material composition analysis.

The principle is in an acceleration of ions in the energy range of keV onto the solid surface of the sample. The impact spot size is affected by the ion beam shape and can reach up to 80 nm for Bi^+ [11]. Primary ions release their energy into the solid via a cascade effect. This interaction is further described in Subsection 2.3.1. Formation of particles from the sample occurs in a vacuum above the surface, e.g., electrons, neutral atoms, clusters,... (see Figure 2.5). Majority of the material is sputtered away as neutrals, however, there is a small fraction of charged particles so-called *secondary ions* (SI) [28], which are analyzed in a mass spectrometer, commonly Time-of-Flight (Subsection 2.3.2). The output of SIMS method is an intensity spectrum versus the mass to charge ratio of sputtered particles.

Modern SIMS instruments operate in various modes. *Static mode* allows the cohesion of the surface to be maintained during an operation before the interval of analysis ends. This means that the primary ion interaction with the volume is not affected by subsequent impinging ions. For a current density in the source it does not exceed $5\,\mathrm{nA\,cm^{-2}}$ in $1000\,\mathrm{s}$. While maintaining other conditions, e.g., fluences below 10^{12} ions per cm^2, it is possible to prolong the lifespan of the outer monolayers up to several hours. Static SIMS exceeds in high sensitivity, mass resolution, and detection limits of ppm or even ppb [15, 28].

During the *dynamic SIMS* mode, the primary ion impact is increased to remove material from the surface of the sample. The operator can work towards a relation between the intensity of SI as a function of sputtering time. A careful calibration can deliver the conversion of time to a formed crater depth [28]. In-depth resolution can reach up to 1.5 nm, but is generally aggravated due to the heavier elements present in the sample.

Many instruments offer dual beam mode. It is the combination of two primary ion sources, placed at 45° angles towards the sample. The TOF-SIMS5 uses the Bi_{1-7}^+ ions as an analyzing beam to create secondary ions, whereas either O^+/Cs^+ or O_2^+/Ar^+ ions contribute to the crater formation. In the first few monolayers, ions mix with the sample material creating an equilibrium causing a constant sputtering rate. This presence of some implanted primary ions can lead to an enhancement of secondary ion yield, making SIMS a remarkably surface sensitive method. Dynamic mode is very useful for the microelectronic industry in dopant determination for up to $\sim 10\,\mu\mathrm{m}$ in depth [11].

2.3.1 Ion-matter interaction

As mentioned above, primary ions, incoming onto the sample, transfer their energy to particles within the surface. Overcoming the bond energy results in an ejection of the material from the solid. The surface binding energy defines the energy required to break a bond between atoms situated at the outer atomic layers of a solid. Approximately, in an unperturbed system, this energy corresponds to the surface potential barrier. This process of material ejection is referred to as *sputtering*. During this event, the creation of both positive and negative, singly and multiply charged (clusters of) particles occur above the surface, simultaneously with neutrals. According to [25], the value of binding energy of microelectronic elements is of the order of 1 eV.

During an interaction with the solid, the primary ion can scatter off the surface, evaporate from the surface, fragment, be adsorbed, or be implanted into the solid in the magnitude of a few µm. Figure 2.5 shows possible outcomes of ion-solid interaction. We consider a model of energy conservation via either elastic or inelastic collisions. During the elastic collision, an ion transfers its energy to another particle in the form of momentum, thus changing its original trajectory. Inelastic collisions affect the electron excitation of atoms that make up the solid. The incoming ion stays on the same trajectory. Initially, target atoms are at rest, however, through collisions, fast recoils are created and set other atoms in motion. Total energy difference dE of an ion on the infinitesimal distance dx is defined as *stopping power* [29]:

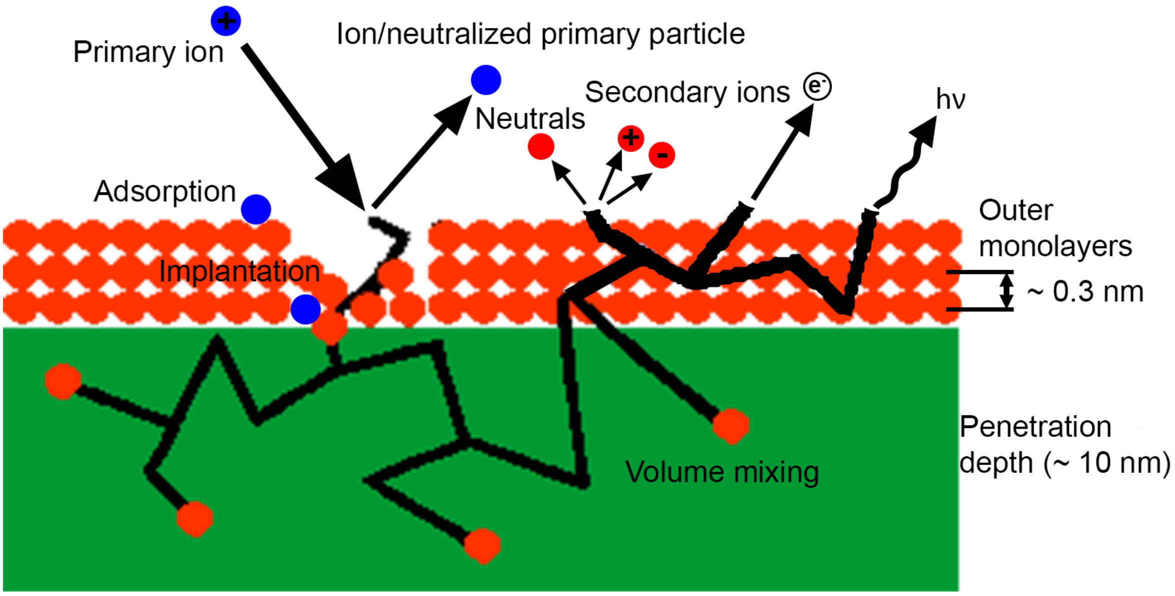

Figure 2.5: Graphic representation of sputtering process with possible outcomes. Adapted from [30].

$$\left(\frac{dE}{dx}\right) = \left(\frac{dE}{dx}\right)_c + \left(\frac{dE}{dx}\right)_e . \tag{2.5}$$

The sum represents the contribution of core and electron stopping power. With the increasing ion energy, the effect of inelastic electron collisions arises.

Series of collisions within the sample result in different forms of sputtering (purely through momentum transfer, through excitation induced by the incoming ion, or a combination of both). Mathematically, to simplify the solution, let's consider only two-particle interaction with no external interference. The relative motion is reduced to a single particle moving in a central potential. Particles in close proximity to each other experience a repulsive Coulomb potential causing the trajectory to deviate from its original path [15]

$$V(r) = \frac{1}{4\pi\epsilon_0}\left(\frac{Z_1 Z_2 e^2}{r}\right)\cdot\Phi\left(\frac{r}{a}\right), \tag{2.6}$$

where Z_1, Z_2 are the atomic numbers of particles in the collision. e is the unit charge, $\Phi(r/a)$ is the screening function defining electronic clouds surrounding the nuclei [31], r is the distance between particles and a is called screening length. Unfortunately, there is no general formula for every type of collision, and the model needs to be adjusted according to electron orbit potentials. For simplification, let's consider our model interaction without the shielding of the electron shell.

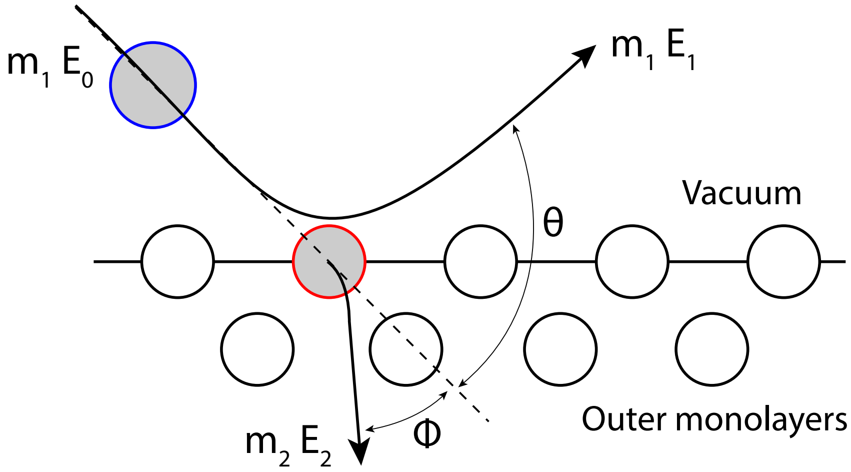

Figure 2.6: Binary collision scheme. Incoming particle m_1 of certain energy is scattered into an angle θ from target particle m_2.

The kinematics of two-particle collisions can be derived from the conservation of energy and momentum before and after the interaction. For an incident particle of mass M_1 and a certain velocity v_0, we can calculate its energy and momentum. After the collision occurs, the final values of energies E_1 and E_2 are dependent on the scattering (θ) and recoil angle (ϕ) as illustrated in Figure 2.6. Considering the target particle is initially at rest, the conservation of energy and momentum is expressed by equation [31]

$$\text{Energy:} \quad \frac{1}{2}M_1 v_0^2 = \frac{1}{2}M_1 v_1^2 + \frac{1}{2}M_1 v_2^2, \tag{2.7}$$

$$\text{Longitudinal momentum:} \quad M_1 v_0 = M_1 v_1 \cos\theta + M_2 v_2 \cos\phi, \tag{2.8}$$

$$\text{Lateral momentum:} \quad 0 = M_1 v_1 \sin\theta - M_2 v_2 \sin\phi. \tag{2.9}$$

One can now determine the ratio of energy and velocity of the projectile particle as:

$$\frac{E_1}{E_0} = \left[\frac{\left(M_2^2 - M_1^2\sin^2\theta\right)^{1/2} + M_1\cos\theta}{M_2 + M_1}\right]^2, \tag{2.10}$$

$$\frac{v_1}{v} = \left[\frac{\pm \left(M_2^2 - M_1^2 \sin\theta \right)^{1/2} + M_1 \cos\theta}{M_1 + M_2} \right]. \tag{2.11}$$

The ± covers both scenarios, where the impinging ion has more (+) or less (−) mass than the target particle. The energy ratio $k = E_1/E_0$ is called *kinematic factor*. This value shows that the energy result of scattering is determined only by the masses M_1 and M_2

$$k = \left(\frac{\pm\sqrt{A^2 - \sin^2\theta} + \cos\phi}{A + 1} \right)^2, \tag{2.12}$$

where $A = M_2/M_1$. The target particle, initially at rest, is scattered into the recoil angle and the energy transfer is given by the relation

$$\frac{E_2}{E_0} = \frac{4M_1M_2}{\left(M_1 + M_2\right)^2} \cos^2\phi. \tag{2.13}$$

Scattered primary or secondary ions can further transfer momentum and affect other particles within the solid. Each collision can be considered as a separate event, thus the simplification mentioned above is sufficient. For calculations with higher ion energies ($E > 100$keV), cluster ions, or screening function considerations, more complex models and even quantum mechanics are necessary.

Ion sputtering

Consider again Figure 2.5. The yield of sputtering is defined as the number of atoms, ions, or molecules removed by a primary ion impact. Particles in the specimen need to obtain enough energy via recoil cascades to overcome surface binding energy (Λ_0). This energy represents the minimum energy of a particle on the outermost surface and only the normal component should be counted. That is, an atom reaches the surface in the direction of 45°, to leave the target, energy required is at least $1.4 \times \Lambda_0$. However, the surface binding energy can vary during sputtering, as incoming ions damage the surface, hence increasing the roughness [32, 33].

Sputter yield differs according to the atomic number[6] Z, crystallography, and experimental geometry (angle of incidence). The value for single-element material can be successfully predicted by theory [34] with respect to the nuclear energy loss in the collision cascade. In the normal incidence, the sputtering yield is expressed as [31]

$$Y = \Lambda F_D, \tag{2.14a}$$

where

---

[6] Sputtering yield is more pronounced for heavier mass target atoms.

$$\Lambda = \frac{4.2 \times 10^{-3}}{N\Lambda_0}, \tag{2.14b}$$

$$F_D = \alpha N S_n. \tag{2.14c}$$

Λ consists of parameters of the target, i.e., surface binding energy, lattice. F_D denotes the density of deposited energy at the surface, α is a correction factor for large-angle incidences, and N is the atomic density of target atoms. Together with the nuclear stopping cross section, Sn gives the nuclear energy loss as stated in Equation 2.5 [31].

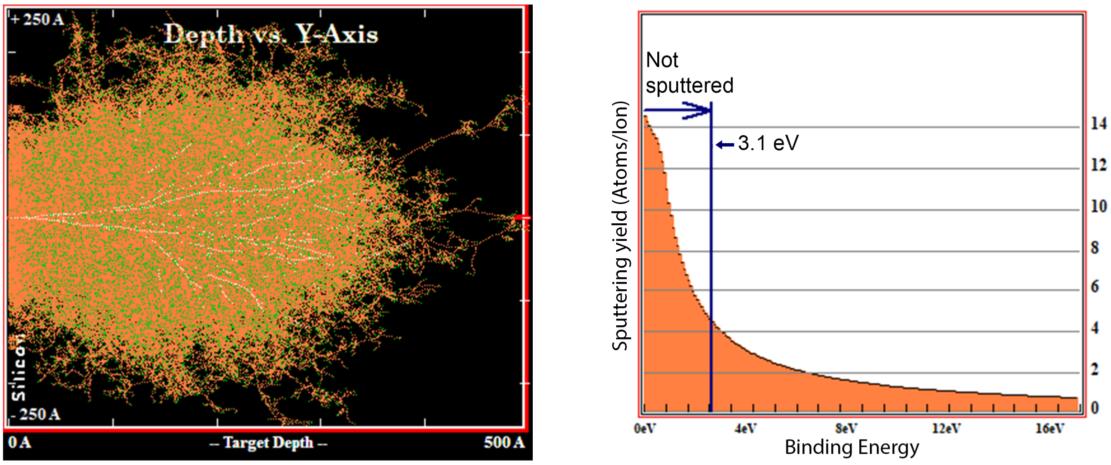

(a) Penetration depth.

(b) Graph of sputtering yield vs energy.

Figure 2.7: TRIM simulation of 30 keV Bi ions sputtering of Si atoms at the normal incidence. (a) Recoil implantation into silicon occur in range of hundreds of Å with orange and green color represents respectively moving and stopped atom. (b) Graph shows the marginal energy of sputtering of Si atoms.

Significant influence on the overall sputter yield can be charge accumulation[7]. Static charge at the surface is balanced by the incoming and outcoming ions and secondary electron production during the collision cascade. With this equilibrium out of balance, charging occurs. This could significantly alter the secondary ion signals and mass resolution. Due to the fact that SI are not accelerated sufficiently towards the analyzer, most instruments use a low energy electron gun, called *flood gun*. These electrons are accelerated towards the sample to compensate the surface charge, although they do not promote the formation of new electrons [28].

Figure 2.7 shows Monte Carlo simulation of 30 keV Bi_1^+ ions targeted at the pure silicon surface in the TRIM computer software. The program focuses on ion interactions and offers different insights on implantation layer mixing and sputtering. Calculation was performed in the collision cascade regime until each primary ion energy drops below the lowest displacement energy of any target atom. In Figure 2.7a, a moving atom is colored orange and green shows a stopped atom. TRIM is also able to compute sputtered particles, which overcame the surface binding energy (Figure 2.7b).

---

[7] This effect is important for insulator measurements.

Secondary particles are atoms/molecules that have gained enough energy to leave the solid's surface. Nevertheless, only a small fraction of the population was ionized. Ionization is the ability of an atom to accept or donate electrons. The most prevalent process is charge transfer. As the wave functions of electronic states extend out from the nucleus, the quantum tunneling can occur. Depending on the energy state difference of donating and receiving atoms, resonance, quasi-resonance, and Auger charge transfer processes are distinguished [15].

All previously mentioned parameters affect a measurable ejected population as stated in the equation

$$J_s = J_p c Y \beta^{\pm} f, \tag{2.15}$$

where J_p is the primary ion current density, c relative concentration of element, β is ionization rate and f is the instrument's transmission function. Most of the parameters are sample dependent. The composition dependence can frequently be neglected if the concentration of an element is below 1%. If not, the effect of the matrix on the secondary ion yield needs to be taken into account.

Matrix effect

The formation of secondary ions is, among other things (Equation 2.15) highly sensitive to the chemical composition of atoms on the surface due to ionization/neutralization processes. This dependence is a significant factor for the signal quality, multilayer depth profiles and further quantification [15]. Several solutions to this problem are conducted in the literature, e.g., measurement of a molecular ion composed of the ion of interest or a deposited silver layer. During the quantification of elemental distributions, the analysis of matrix-matched reference materials is carried out to take the matrix effect fully into account. This is called Relative Sensitivity Factor (RSF) approach [35].

2.3.2 Time-of-Flight mass spectrometer

Mass spectrometers are an integral part of any SIMS instrument, which relies on the ability to distinguish secondary ions by mass to charge ratio. And since the vast majority of ions emanate in the $+1$ or -1 charge state, it is safe to establish the mass resolution of these detectors. TOF-SIMS5 in CEITEC Nano facility is using Time-of-Flight spectrometer. It exceeds its competitors in high mass resolution and sensitivity, especially aimed for static and shallow dynamic SIMS [28].

Ions extracted from the specimen are drawn towards the spectrometer by applied voltage, positive or negative depending on the SI polarity and measuring regime. In the analyzer, ions are subjected to an extraction field V_e and accelerated to the same kinetic energy E_k given by $E_k = qV_e$. Energy is constant for all ions, the velocity is inversely proportional to the mass:

$$qV_e = E = \frac{1}{2}mv^2. \tag{2.16}$$

If the flight path is kept constant, the time it takes to reach the detector is derived from the equation

$$t = \frac{L}{v} = L\sqrt{\frac{m}{2qV_e}}, \tag{2.17}$$

where L is a path length. In the instrumentation setup, the energy filter is used to ensure the shortest time difference for ions with the same m/q ratio. Such filter can be created with reflection electrodes placed in the spectrometer tube. This deflects particles with different kinetic energies but the same m/q, thus increasing their trajectory and time of flight. To sum up, lighter ions reach higher velocities and consequently, heavier ions travel more slowly [15, 36].

Mass resolution is, in fact, one of the most important SIMS' features. It is the instrument's ability to distinguish a signal of two similar masses with a difference Δm. It can be found by error propagation of uncertainties [28]

$$\frac{\Delta m}{m} = 2\frac{\Delta t}{t} + \frac{\Delta E}{E} - 2\frac{\Delta L}{L}, \tag{2.18}$$

where Δ are uncertainties of time, energy, and flight path length. The mass resolution varies mostly with the time factor, i.e., the primary ion beam pulse width, response time of the detector, and time resolution of the detector. The main influence is the pulse width, hence this is the reason for pulsed ion beams in SIMS. Continuous beam is being deflected to the small aperture achieving ~10 ns. Furthermore, to improve the accuracy of the spectrometer, a beam buncher is present in the primary beam column. A set of electrostatic lenses decelerates ions in the front and accelerates ions in the back of the pulse, resulting in 1 ns interval.

2.4 Scanning Electron Microscopy

Prof. Ondřej Křivánek once said *"Electron microscopy is the eyes of science."* [37]. And that is true. Scanning electron microscopy (SEM) was originally invented for the magnification of objects invisible to the human eye. As the visible light microscopy is limited by the wavelength, according to the Abbe's formula, SEM achieves better resolution. The de Broglie wavelength of electrons is [38]

$$\lambda = h/mv = \frac{hc}{(2EE_0 + E^2)^{1/2}} \tag{2.19}$$

where h is Planck's constant, m denotes the relativistic electron mass, $E_0 = m_0c^2$ rest energy and kinetic energy $E = eV$. Yet, the influence of relativity on mass and velocity is small for electron energies below 50 keV. For instance, the wavelength λ is 6.98 pm for 30 keV. This gives us the value of resolution about five orders of magnitude lower than for light. However, the actual limits are crucially affected by optical aberrations.

The first electron microscope ever built was in 1931 by physicist Ernst Ruska[8]. The principle of SEM is in electrons targeting a specimen and following detection of the sample response. Electron beam from a thermionic, Schottky, or a field-emission cathode is accelerated by a voltage in the extent of 0.1–50kV and focused via a set of apertures, electrostatic and magnetic fields. So that an electron probe diameter in units of nm and a certain beam current can be formed at the specimen surface.

2.4.1 Electron-matter interaction

As mentioned in Subsection 2.3.1, elastic and inelastic scattering are elementary atomic interaction processes. The consequence of a *primary electron* (PE) interaction with surface atoms is composed of many complementary outputs from different sample depths (see Figure 2.8).

Energy spectrum of the emitted electrons consists of secondary electrons, *backscattered electrons* (BSE) and *Auger electrons* (AE). The SE are generated by inelastic collisions to high energy levels of an atom. Excited electrons can overcome the work function and leave the sample from a depth of up to 10 nm. SE high-resolution topography images are frequently used, as the detection of slowly traveling electrons is fairly easy and the yield is sufficient. A positively biased grid is placed on the side of the specimen and electrons are collected via a scintillator.

BSE are the primary electrons that suffer from elastic collisions within the bulk causing them to decelerate. Conventionally, the limit to distinguish SE from BSE is the energy of 50 eV. AE are the result of ionization of an inner shell. The subsequent de-excitation energy released due to the electron transition from the upper shell is converted to another atomic electron. Electrons released from the sample by this Auger production method come from the outermost atomic layers, thus offering valuable surface-sensitive information including the spectroscopy measurement of its characteristic kinetic energy [39].

---

[8] Although this was the TEM type.

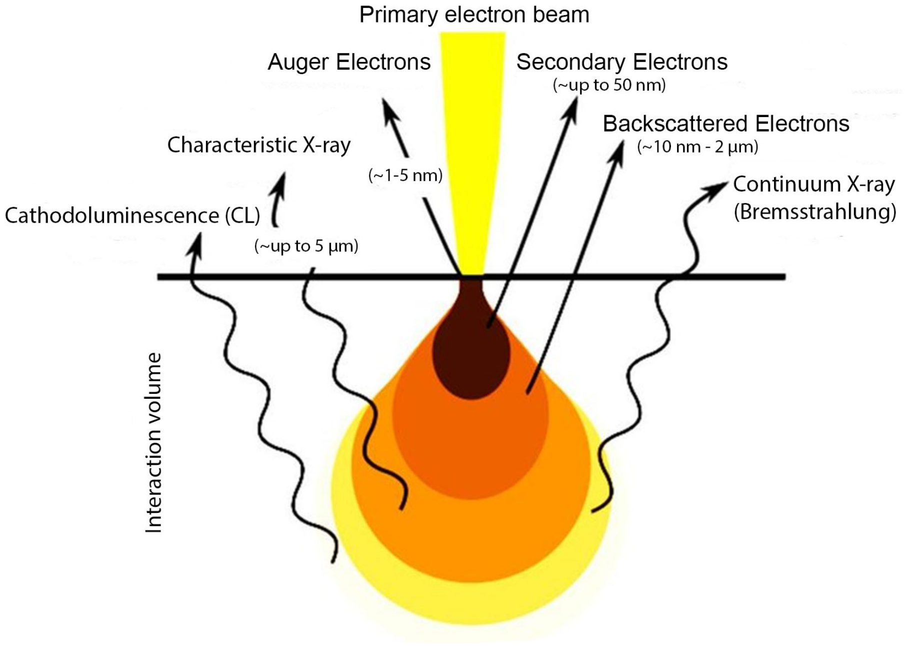
Primary electron beam
Auger Electrons
Secondary Electrons
(~up to 50 nm)
Backscattered Electrons
(~10 nm - 2 µm)
Characteristic X-ray
(~1-5 nm)
Continuum X-ray
(Bremsstrahlung)
Cathodoluminescence (CL)
(~up to 5 µm)
Interaction volume

Figure 2.8: Primary electron matter interaction scheme. Representation of the complementary signals with depth of origin. The penetration depth is highly dependent on the primary electron energy and sample composition. Adapted from [40].

2.4.2 Energy Dispersive X-ray Spectroscopy

As Figure 2.8 suggests, after the primary electron impact and interaction with the volume, the sample's response consists of various outputs, among which are photons. The primary beam scans point by point on the surface, X-rays emerge at each location and can provide a chemical identification of the elements present. The physics behind this phenomenon is defined very well.

The process of X-ray generation and other atomic interactions is illustrated in Figure 2.9. At first, the primary electron energy must exceed the binding energy for the particular energy level electrons. Experimentally speaking, for a sufficient intensity of the characteristic radiation, E_0 of the PE must be at least twice as large as the critical excitation energy to generate X-rays [41]. An incident electron beam inelastically scatters with an inner shell atomic electron. If sufficient energy $E_0 > E_c$, E_c being the critical excitation energy, is transferred to the electron from the inner shell, it is ejected from an atom. The energy of this outgoing electron is described as the difference between the primary electron energy, ionization energy, and additional kinetic energy (E_k) imparted [39]:

$$E_{out} = E_0 - E_c - E_k. \tag{2.20}$$

The ionized atom is left with a vacant place and a raised energy state. The outer-shell electron relaxes to the ground state. The excess energy released is in the form of X-ray emission[9]. The carried energy of the photon is the difference between the ionization energies of the two orbitals involved [39]:

---

[9] Or as previously briefly mentioned via Auger electron ejection.

$$E_{X-ray} = E_{inner} - E_{outer}. \tag{2.21}$$

As X-ray transitions correspond to a certain element, by measuring the energy with respect to E_0, the sample chemical composition can be derived. There are unfortunately obstacles. As opposed to secondary electrons, X-rays are collected from the largest volume beneath the surface due to the cascade excitations related to the element. On the way to the detector (mostly SDD), X-rays propagate through a large range of depths, thus are subject to absorption, signal intensity reduction and parasitic X-rays (see Subsection 4.2.1) [42].

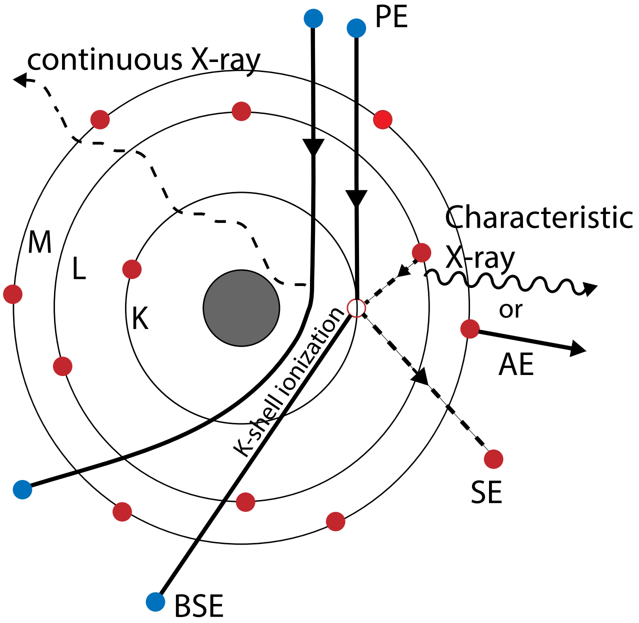

Figure 2.9: Schematic diagram of excitation and de-excitation mechanisms leading to the X-ray generation. Lighter atoms can experience the Auger effect instead. Based on figures from [41, 43].

Apart from the characteristic X-rays, a continuous X-ray called *bremsstrahlung* is introduced into the energy spectrum. When electrons enter the Coulomb field of an atom, they will decelerate and the loss of electron energy emits as a photon. These X-rays form a spectral background beneath the characteristic peaks and alter the accuracy of measurement.

3 THROUGH-SILICON-VIA

All 2D and 3D measurements in this thesis were performed on various Through-Silicon-Via (TSV) samples. This chapter is dedicated to the brief explanation of the functions, fabrication, and reasons for failure analysis of TSV structures.

Three-dimensional integrated circuits are considered as promising candidates to replace the conventional 2D arrangement and overcome the limitations of Moore's law. In particular, the transistor shrinking is not everlasting and the laws of physics eventually intervene, i.e., electron tunneling and heat dissipation, thus the cost and manufacturing difficulty rise. 3D IC reports lower power consumption, higher performance, and function density. TSVs are devices joining semiconductor circuits or devices stacked either on top or next to each other to create electrical and mechanical connections and provide power supply (see Figure 3.1) [44].

The so-called *die* is part of a silicon wafer with circuit. These have been attempted to interconnect many times by wire loop or flip chip bonding [45]. Yet TSV provides a shorter electrical path, less signal delay, and thinner packaging. The concept of chip stacking dates to the 1960s, however, any significant applications were proposed at the turn of the millennium. It is being researched and developed for various technology applications such as CMOS image sensors[1] (the type of TSV analyzed in this thesis), MEMS, and memory devices.

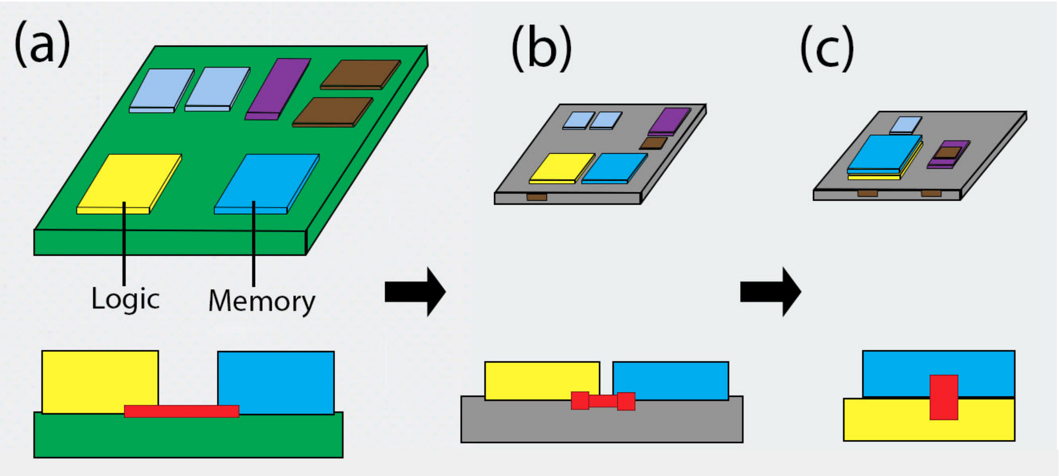

Figure 3.1: Packaging technology of IC. (a) traditional package; (b) 2.5D die stacking next to each other via TSV; (c) full 3D TSV stacking of logic and memory device. Not to scale. Adapted from [45].

---

[1] Compared to CCD, at CMOS sensor there is enough space for ADC at each pixel. Every component is integrated and can provide faster readout than CCD.

3.1 TSV fabrication

The fabrication is divided into 3 types depending on the order of TSV creation compared to the rest of the chip. *Via first* means the TSV was etched into the wafer before the front-end-of-line (FEOL) and back-end-of-line (BEOL). This consist of annealing, junction creation (transistor), interconnection, and followed by wafer thinning. The challenge of this method is the risk of TSV fill diffusion into the surrounding material as a result of high temperature during annealing [46]. In the *Via middle* process, TSV is fabricated between FEOL and BEOL build. *Via last* approach fabricates the TSV latest, where the challenge lies in TSV alignment at the exact position. The choice of TSV fabrication as well as dimensions are based on the final application requirements of a particular device [44].

3.1.1 Etch process

Formation of via consists first of etching a trench into the silicon substrate 5–400 µm deep with the high aspect ratio depending on the chip application (Figure 3.2b). The process is typically executed by so-called *Bosch etching* [44], [45]. Fast isotropic Si etching is utilized by SF_6. Though, TSV require highly anisotropic etch. This is achieved by deposition of a passivation layer on the sidewalls to protect the silicon substrate from lateral etching. Additional ion bombardment plasma etching dissolves the passivation layer at the bottom of the via and allows SF_6 to deepen the trench. This continues repeatedly until the desired depth is accomplished.

Bosch etching reaches fast milling speeds on account of sidewall roughness [47], which may introduce reliability issues (see Section 3.2). The profile is demanded to be uniform and vertical with minimized horizontal deformation.

3.1.2 Protection layer

Metal-filled TSVs require proper electrical isolation from the surrounding bulk Si to prevent electrical breakdown [48]. SiO_2 or Si_3N_4 are generally used as an insulation barrier with good step coverage and thickness uniformity, low leakage current, high breakdown voltage, and ability to withstand processing temperatures (Figure 3.2c). Conformal coverage ($\sim 100\,\mathrm{nm} - 1000\,\mathrm{nm}$) of oxides is carried out by chemical vapor deposition (CVD) [45].

The following step is the barrier layer deposition, which prevents the fill to diffuse into the oxide or silicon during annealing. The most commonly used materials are Ti, TiN, Ta or TaN utilized by physical (PVD) or chemical vapor deposition (Figure 3.2d). Typical thickness is tens of nanometers.

3.1.3 Metallization

The requirements for the conductor inside a TSV are low resistivity, good thermal conductivity, void-free fill, and minimal stress (Figure 3.2e). The common materials are Cu, W, or doped polysilicon [45]. For the via-middle process applications, Cu is used for its low resistivity (1.7 µΩ cm) and thermal dissipation. The Cu seed layer is adapted by physical vapor deposition and a fill (if present) by electroplating. Wafer is immersed into a solution containing, among other additives, cupric ions. Next, a current is passed through and deionization occurs. Excess copper is then removed by chemical and mechanical polishing (Figure 3.2f) [46]. TSVs studied in this thesis contain the metallization layer on the walls of the trench, without the fill.

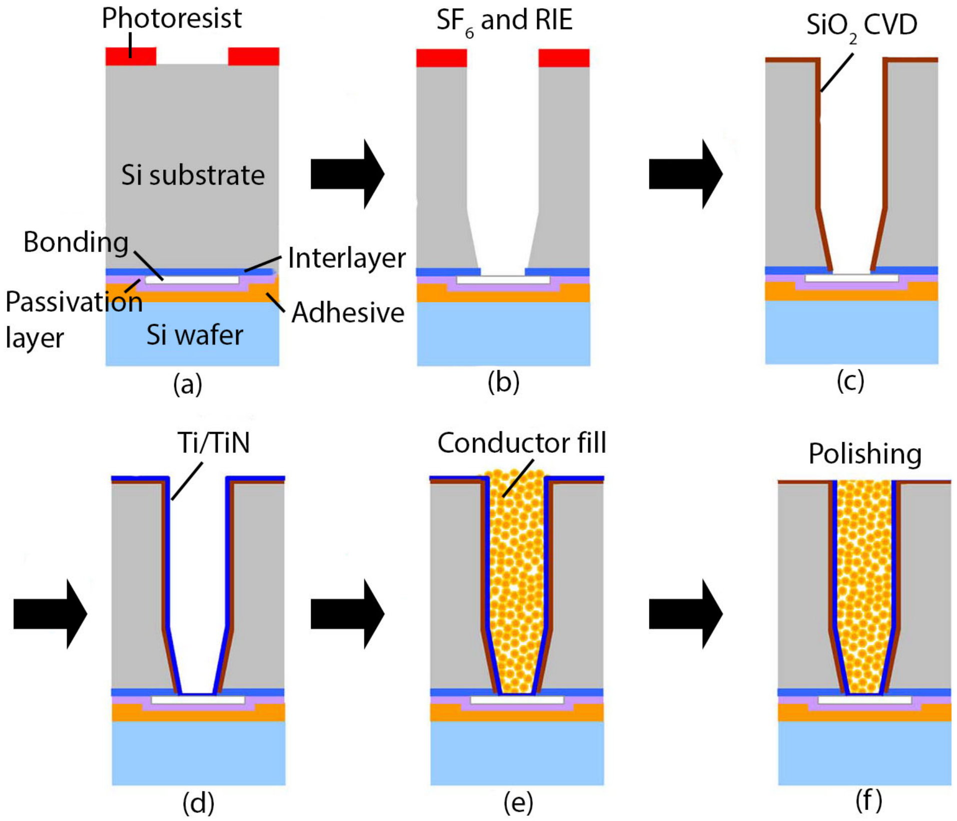

Figure 3.2: Process flow of TSV fabrication. (a) Etching preparation, litography; (b) Si etching by an etchant in combination with reactive ion etching (RIE); (c) insulator barrier deposition; (d) diffusion barrier deposition; (e) conductive seed layer fill; (f) excess copper and barrier removal. Adapted from [46].

3.2 TSV inspection

As TSVs are gradually becoming an essential part of integrated circuits, the requirements for stability and reliability grow. Any malfunction can fail the die, if not the whole device, as a result of power supply and signal delivery. Main issues with TSV are caused by undesirable side effects during ion etching and metallization layer consistency.

At first, the actual trench needs to be monitored, its depth uniformity and profile. Sidewall roughness, called *scalloping* [44], caused by reactive ion etching, can induce poor step coverage of the following processes resulting in electric field enhancement, hence causing leakage or breakdown. Any irregularities in the horizontal deformation can also affect the following fabrication steps, such as the barrier film thickness. TSVs can be examined by SEM cross-section or infrared (IR) illumination [45] of the wafer backside.

Secondly, the issues occurring during die annealing are caused by different thermal expansion of silicon and copper, resulting in mechanical stress, which can lead to deformation of the layers above TSV. It is important to keep the temperature relatively low to minimize copper extrusion [45] and possible diffusion into the bulk silicon. These defects are the origin of the resistance increase of a circuit. It is possible to detect them by measuring V/A curves and to confirm by spectral analysis of cross-section by SIMS or EDS.

Apart from temperature influence, electromigration plays an important role in TSV failure. As electrons in a conductor move towards anode as a result of potential differences, they impart momentum to the lattice atoms causing atom migration toward anode [45]. This motion can deplete the metal atoms at one side of the wire and consequently voids are occurring. Voids large enough can cause the circuit to fail. The formation of voids and bumps can happen during PVD-Cu seed deposition as a result of scalloping [44]. Physical irregularities of TSV are measured by X-ray computed tomography [49, 50].

4 2D AND 3D MEASUREMENTS

The second part of the thesis addresses the actual 2D cross-section and 3D tomographic analysis by selected techniques of NanoXCT, FIB-SEM (EDS), FIB-SIMS, and AFM. Additionally, the data processing and results correlation is outlined, but will be described more in detail in Chapter 5. NanoXCT study has been performed in advance in Fraunhofer IKTS. However, part of this thesis are the CT results, which were further processed by the author into a form usable in a correlative study. It is hoped that this thesis will contribute to a better correlative approach to the analysis of semiconductor structures.

4.1 NanoXCT data

The basic physical principle, on which X-ray Computed Tomography is based, allows scanning samples independently on the size. The radiation that passes through the bulk loses some of its intensity due to the absorption mechanisms depending on the thickness and composition of the material. Therefore, its unique properties make it possible to reconstruct the skeleton of the sample non-destructively. All CT measurements were performed at the Fraunhofer IKTS under the supervision of Dr. Jürgen Gluch.

Nano-XCT study used a Xradia nanoXCT-100 device from Xradia Inc. The sample is illuminated with a parallel beam geometry and with additional optical elements enlarge the image. The system operates with monochromatic X-rays of 8 keV energy (Cu-K_α) in the absorption phase contrast mode. Exposure time is 160 s per image with hundreds of projections. Raw results were reconstructed by Dr. Jürgen Gluch in Tomo3D software [51].

Despite the area of interest being hidden beneath the outer layer, which is the remnant after the lift out from the die, the first results give a look at the TSV itself. Figure 4.1 reveals the core in the surrounding packaging of the sample with designation *sample 9*. Individual CT scans were stitched together creating an overview for better perception.

The TSV stretches over the whole wafer thickness. The back side of the TSV (situated at the bottom of the image) is hollow. This cavity passes through the wafer and is closed below the surface at the front side of the TSV (topside of the image). The metallization of the TSV (Subsection 3.1.3) is expected to be on the sides of the crater.

At first glance, it can be seen that the uniformity of the profile was not achieved. A large bubble about 40 µm in size appeared near the front side. Additionally, the surrounding seems broken, partially exposing the inner parts. The clean cut leads to the conclusion that the deformation appeared during the sawing process. Further research

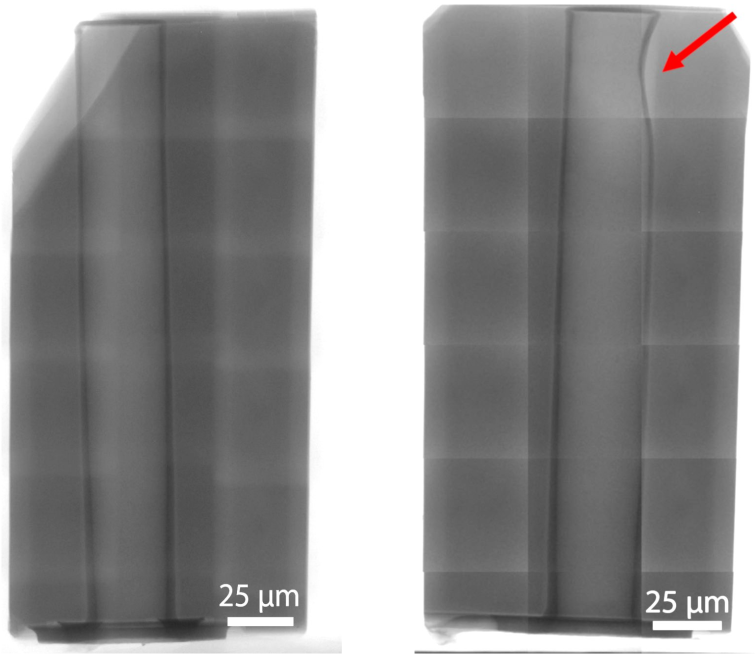

(a) 0 degrees (b) 90 degrees

Figure 4.1: Images represent a pillar containing a sample 9 TSV with a front and a side view. CT scans are stiched together into mosaic 3×6. At the 90° rotation, the breach of the uniformity of the inner cylinder is visible. Courtesy of Fraunhofer IKTS.

will be needed to discover deeper disorders and clarify the origin, shape, and filling (if any) of the bubble.

Depending on the detector, X-ray CT is normally not able to achieve a resolution better than 1×10^{-3} times the sample size [5]. Therefore additional CT measurement of the region of interest was performed, thus improving the signal to noise ratio. High resolution imaging of the deformation area (60 µm long part) was analyzed with $130\,\text{nm}^3$ voxel size. The virtual slices are illustrated in Figure 4.2 and for the most part represent the front side with the closed cavity. Apart from the bubble disorder of the core, the outer layers are clearly deformed. This is shown by the different shades of gray. This contrast is most noticeable in the slice of the XY plane. The interface between the darker and lighter parts indicates a crack or a defect in the outer layer.

Consider Figure 4.3. A 3D model of the ROI was created by the author from the obtained CT data from the Fraunhofer IKTS. In the commercial data visualization and analysis software *Avizo 8.1* [52], the individual slices were segmented by thresholding[1]. The bright voxels of TSV core are visible and the surrounding is assigned as transparent. Consequently, the corresponding model of the TSV front side was created with the *Volume Rendering* function. Dimensions of the TSV were extracted from CT slices[2] and imported into the Avizo, so that the model is up to scale.

---

[1] The segmentation technique of clustering of pixels with similar intensity value. Pixels in one class are assigned with a value 1 while the rest has a value 0 [53].

[2] Later on dimensions were compared to SEM images to precisely co-register both methods (Subsection 4.2.3).

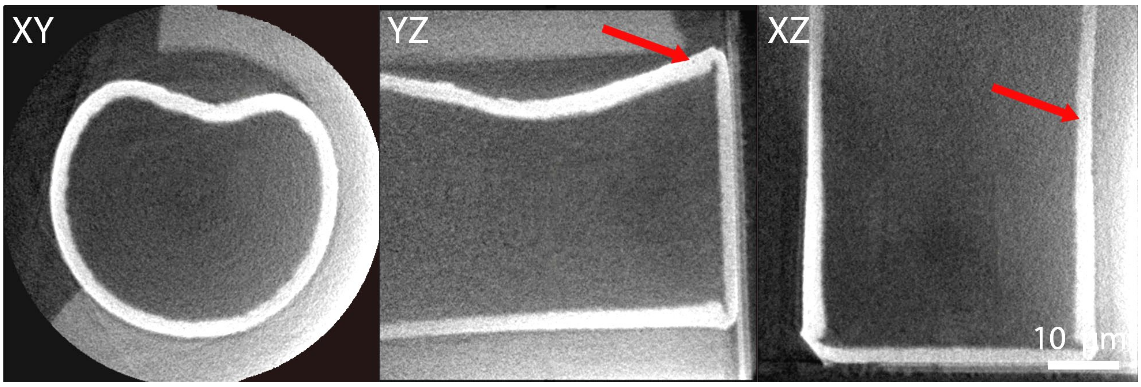

Figure 4.2: Sample 9 X-ray tomography slices of the front side part with the closed cavity. Red arrow marks some pores in an inner layer. Slices reach up to the bubble flattening ≈60 μm from the topside of Figure 4.1. Courtesy of Fraunhofer IKTS.

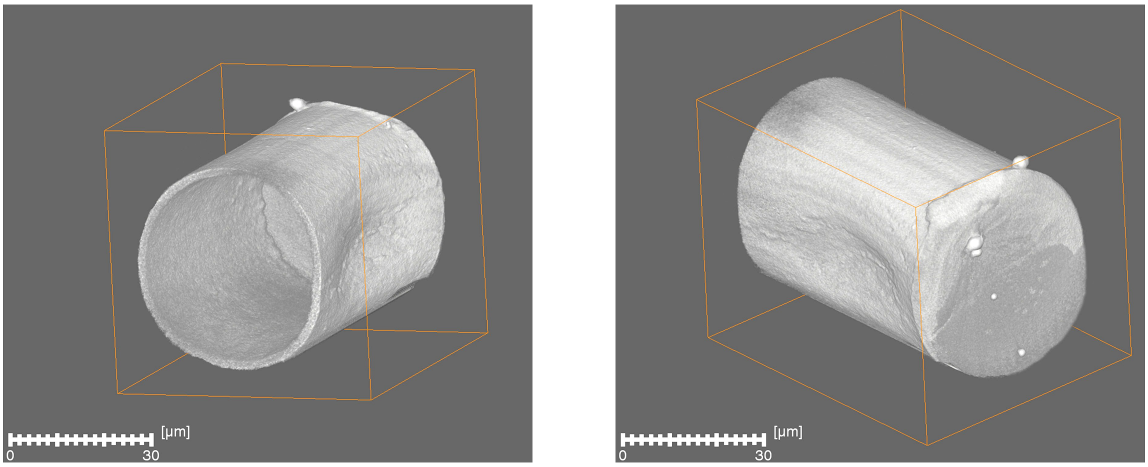

Figure 4.3: 3D model of the front side part of the TSV sample 9. Rendering and segmentation from CT slices has been done in the Avizo 8.1 software.

It is clearly visible that the sample 9 itself consists of a metallized core layer accompanied by a hollow cavity, as previously mentioned. Along this layer it is also possible to observe elongated pores in passivation. Another finding provided by the model are beads at the TSV closure region. These beads are fiducial markers made of Au. Fraunhofer IKTS places them on every sample to align the individual images of the tomography data set before reconstruction.

The *slice* function and the *set plane* option in Avizo was employed (Figure 4.4) to simulate the subsequent FIB cut. According to a normal and a point, a section was defined to form an angle of 45° with the XY plane from Figure 4.2. This area and its orientation were carefully chosen due to the geometry of ion beam columns in the TOF-SIMS5 microscope in CEITEC laboratories and the sensitivity of the SIMS method (see Section 4.3). Milling in this arrangement makes it possible to observe the cross-section and the in-depth development of the bubble by all upcoming methods.

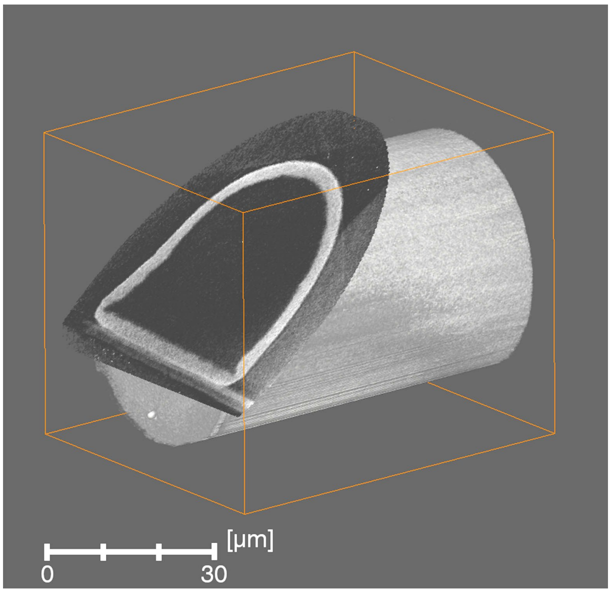

Figure 4.4: Simulated FIB cut of the sample 9 CT data under 45° in Avizo software.

4.2 FIB-SEM (EDS)

Comparing other 3D microscopy techniques (see Figure 1.1), FIB tomography is rather new method and takes its place as a technique achieving high voxel resolution with a relatively large analyzed volume of material [6]. Modern dual-beam apparatuses are equipped with both electron and ion columns to precisely modify and simultaneously view the sample. With the attachment of other detection systems such as EBSD or EDS [54], acquisition of crystallographic and chemical 3D-information is enabled. This section intends to give a short introduction to the background of FIB-tomography (Subsection 4.2.1) and proceeds with high resolution microscopy of sample 9 TSV. CEITEC Institute offers two dual-beam instruments, TESCAN LYRA3 and FEI Helios NanoLab 660, which were employed in this thesis.

4.2.1 FIB serial sectioning

Figure 4.5 illustrates a model view of a microscope chamber during FIB serial sectioning. The angle between the electron and ion beam columns is 52° (in FEI Helios), so the stage is tilted in such a way that the ions are oncoming perpendicular to the sample. The principle of tomography using the focused ion beam is in scanning the cross-section of the sample by available detectors (SE, BSE, EDS, SIMS) and gradually milling down layers of this plane line by line. An example of such cross-section is shown in Figure 4.6. The goal of serial sectioning is the production of a regular stack of images, which is then processed into a 3D model of the sputtered area by stack alignment and image registration.

Even though FIB tomography is a time-consuming technique itself, additional sample preparation is necessary. If a ROI is below the surface of the planar sample, the volume of interest to be analyzed should be isolated from the surrounding material. About 50 μm wide trenches are sputtered around the cube (Figure 4.6) to make the electron beam available to view the cross section and avoid the shadowing effect in the lower

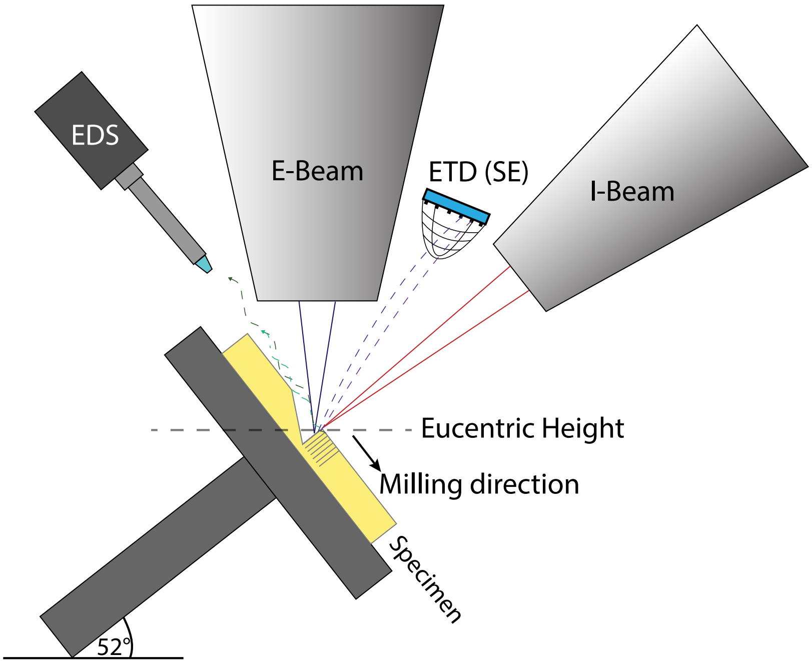

Figure 4.5: A model of dual-beam arrangement for cross-section and tomographic measurement. FIB column is tilted by 52° from electron beam. Secondary electrons (Everhart-Thornley detector) and characteristic X-rays (SDD) can be collected at each slice. Eucentric height is the stage position, where the imaging plane does not change during tilting. Based on figures from [6, 54].

areas of the images [7, 54]. Another reason is faster milling speeds and reduction of resputtering processes.

While measuring EDS maps at each section during tomography, the signal to noise ratio is highly affected by the parasitic X-ray production. The photons from the cross-section are emitted in all directions. If any photon or BSE hits the side wall, it can start the generation of new parasitic X-rays and consequently affect the collected signal count (Figure 4.6a). By increasing the size of the surrounding trenches, the parasitic X-rays are reduced. To completely suppress this noise, lift-out technique has been proposed [55]. The cube is separated from the surrounding specimen via nano-manipulator attachment by the FIBID.

Another sample preparation step is the protection layer deposition. A gas of either Pt, W, or C (depending on the precursor available) is introduced into the chamber using a gas injection system (GIS). After its decomposition into volatile and nonvolatile components by the ion beam, the metal or carbon remains as a few µm thick deposit on the surface of the analyzed area. This helps to reduce FIB milling artifacts (curtaining Subsection 5.1.2, or rippling[3]) and to protect the surface from being sputtered away.

In the beginning of an experiment, depending on the microstructure size, the slice thickness, magnification, and acceleration voltage need to be optimized. It is important to bear in mind the targeted penetration depth in addition to the sufficient PE energy for the X-ray ejection. As mentioned in Subsection 2.4.2, low energy electrons are not able to supply enough energy to the inner shell electron ejection.

---

[3] Rippling are a plateaus in the cross-section of particular semiconductor samples. The origin is attributed to surface perturbations caused by spatial variations in sputter yield. One of the proposed reduction techniques is masking [56]. Region of interest is covered with a thick piece of silicon wafer placed by a nanomanipulator, which aids the overall homogeneity during milling.

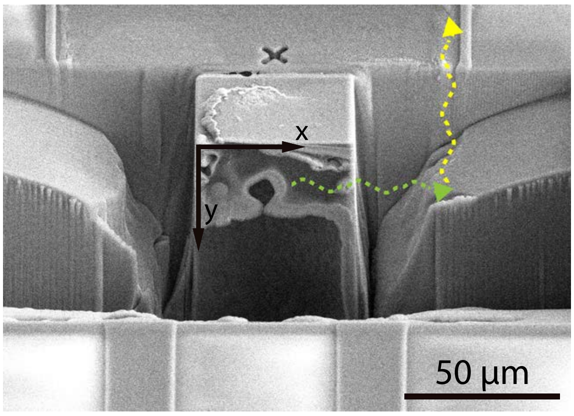

(a) SEM view.

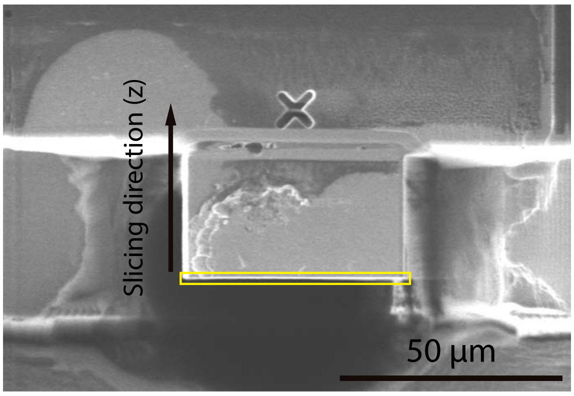

(b) FIB view.

Figure 4.6: Electron (a) and ion (b) beam view of milled down trenches surrounding the ROI for tomographic measurement (in this case front side of a random TSV embedded within a die). (a) also marks parasitic X-ray creation. The depth of measurement was set to 30 µm. The protective layer is not essential, as metallic and other TSV layers are hidden well beneath the surface. The *X* mark is a ion beam tracking fiducial for the *Slice & View* software included in the Helios microscope.

4.2.2 TSV sample preparation

Samples required for correlative study by multiple methods need to be adapted to suit all equipment. Supplied TSV are placed with an adhesive on a steel pin (Figure 1.2). Although this geometry is for X-ray tomography advantageous, as it is easier to rotate the specimen and the lack of the surrounding bulk offers a certain facilitation of data processing, for other instruments it is not so much. This configuration was tested in FEI Helios NanoLab 660 and in TOF-SIMS5. A simple cylinder holder was manufactured, which would keep the TSV in a stable position and would also support stage tilting. Unfortunately, this geometry turned out to be inefficient, as it exceeds the allowed height of the loadlock in the Helios microscope, thus the main chamber would always have to be vented to insert the sample.

In contrast to TOF-SIMS, the sample fits well in the backmount holder, nevertheless other complications occurred. Secondary ions after leaving the sample's surface are affected by the potential field of the time-of-flight analyzer. These equipotential lines copy the shape of the sample (Figure 4.7a). As the TSV is at the tip, the gradient of these lines increases. The trajectory of the particles emerging from the sides of TSV block is thus deviated. If the gradient of equipotential lines is substantial, the SI may be deflected in such a way that they miss or hit the wall of the analyzer (Figure 4.7b). As a result, the overall sensitivity and SI yield are highly reduced.

Several possible solutions have been proposed to increase the yield of secondary ions. The procedures mainly focused on decreasing the step size between the TSV and some planar surface. For example, it has been attempted to pass the TSV through a 300 µm hole in aluminum foil or a TEM grid with 425 × 425 mesh size. Both experiments were inefficient and did not improve the SIMS sensitivity. Surprisingly, the solution turned out to be a simple removal of the TSV from the steel cylinder. Originally, we wanted to avoid this approach, as the dimensions of the TSV are in hundreds of µm and manual manipulation on such a sample is very risky. Eventually, after the acetone dissolution of the adhesive, the TSV has been carefully placed on a silicon wafer with a pair of tweezers. The rotation was crucial, as the ROI needed to be on the top. In conclusion, this geometry provided a sufficient signal increase and in addition the sample could also be inserted into the electron microscope via a loadlock.

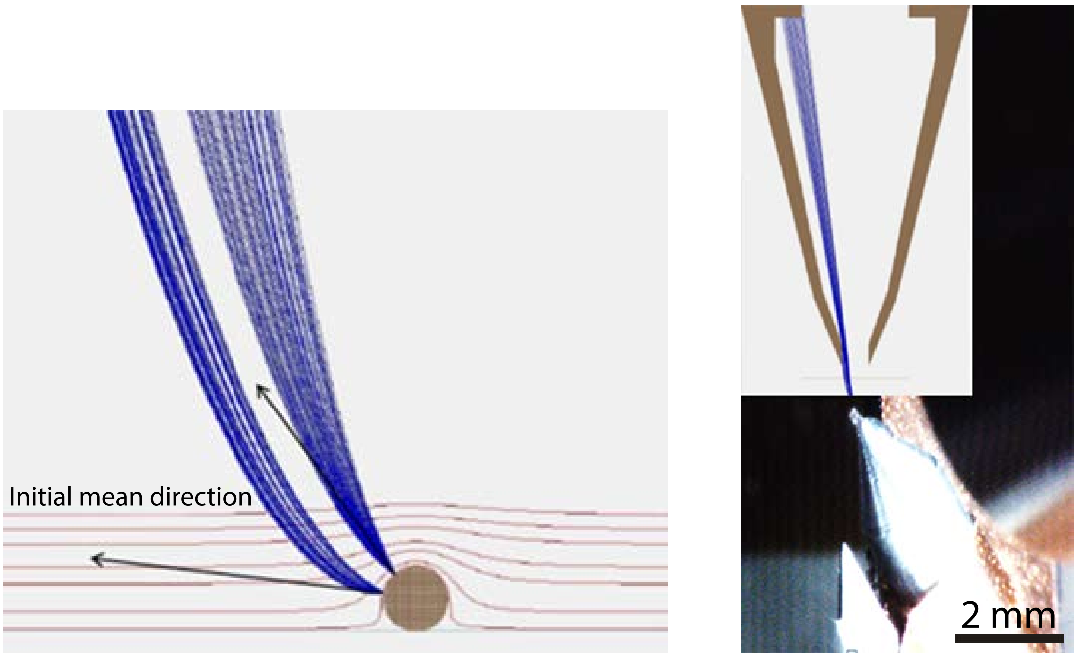

(a) Equipotential lines simulating a particle on the surface.

(b) Camera chamber view with projected particle trajectory.

Figure 4.7: Explanation of sample shape importance in TOF-SIMS. (a) Simion8 simulation of two particle trajectory leaving the surface of elevated sample from different positions. (b) TOF-SIMS camera view of TSV sample 9 with simulated collision of ejected ions with analyzer wall. The concept of images was adapted from 2018 Iontof Summer school presentation.

4.2.3 Sample 9 FIB-SEM

Once the sample was fixed on the wafer, the next step in the correlative study was pursued. According to Figure 4.1, the approximate position of the volume of interest (VOI) was known and the FIB cut was carried out. 30 keV LMIS Ga ions incoming to the TSV at 45° angle with 20 nA beam current gradually milled down the object towards the ROI, as predicted in the simulated FIB cut in Figure 4.4.

Figure 4.8 provides the first SEM observation of TSV sample 9 after the FIB cut to the desired depth. Imaging was performed with 15 keV electron beam with secondary electron detection. Dimensions of the specimen are: ∼300 × 150 × 150 µm with 40.5 µm diameter of the core. It is possible to observe the cavity passing through the entire TSV. Additionally, there are visible remnant stains from the adhesive connecting it to the steel pin (Figure 4.8b). Minor deformation on the surface is probably caused by a pair of tweezers during manual sample transfer (Figure 4.8a).

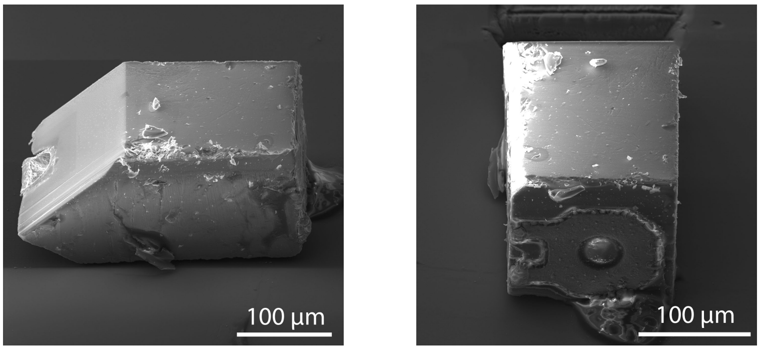

(a) Side view. (b) Back side view.

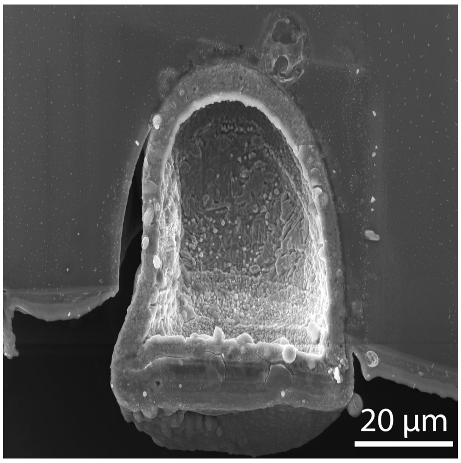

(c) Cross-section.

Figure 4.8: SE images of TSV sample 9 with 45° milled down front side to reach the bubble deformation.

Zoomed in area of the exposed TSV core is shown in (Figure 4.8c) The stage is tilted 45° so that the oncoming electrons are perpendicular to the sample. Investigation of finer scale features specifies the profile asymmetry. A gap between the metallization layer and the surrounding packaging has been formed. This may indicate a poorly deposited passivation layer or anisotropic etching at the bottom of the TSV. The metallization layer with thickness of ∼4 µm appears to be relatively constant with no delamination processes. However, some droplets and dots are visible on the surface. The protective layers might be prone to oxidation. It would be useful to examine the topography of certain parts of the cross-section using AFM method (see Figure 4.10).

Cross-sectional EDS

FEI Helios microscope has a manually retractable energy dispersive X-ray spectroscopy detector. This SDD from EDAX company provides a chip area of 50 mm^2 and an energy resolution of 129.5 eV. Figure 4.9 presents EDS qualitative chemical composition of the sample. Recovered characteristic X-rays of various elements were separated from parasitic X-rays and noise and plotted into an energy spectrum. Amplitude of a specific element is determined by converting the photon energy into electrical signals by EDAX system software. As a result, a graph of intensity (counts) versus transition energy is created.

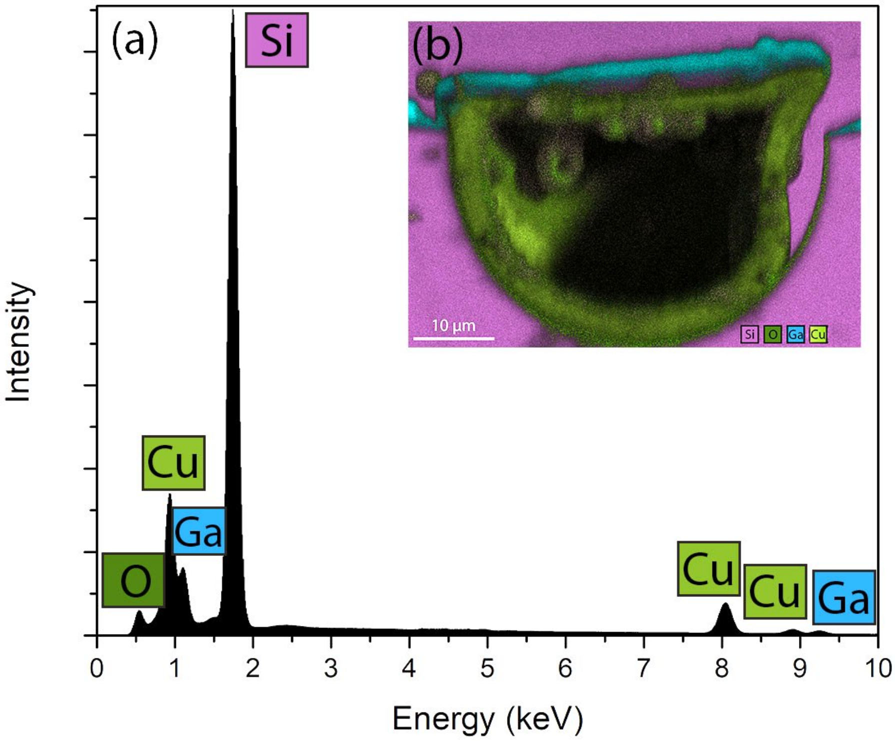

Figure 4.9: Elemental analysis of TSV sample 9 cross-section using EDS method. (a) represents energy spectrum of present elements, (b) overlaid spectral mapping.

As a consequence of the random X-ray generation direction, the orientation of the analyzed area can play an important role in the magnitude of the signal, especially for elements with a lower concentration in the matrix due to the signal to noise ratio decrease. As a result, the stage was oriented towards the EDX detector, thus the spectral map appears vertically flipped in comparison to the the zoomed-in SE image Figure 4.8c. Furthermore, different stage tilts[4] and accelerating voltage were tried to achieve the highest X-ray generation and directionality. The graph set out in Figure 4.9 was obtained with electron landing energy of 10 keV, 0.2 nA beam current and 45° angle of incidence. The measurement was performed in 128 frames with 200 ms dwell time.

---

[4] Electrons incident perpendicularly and at an angle of 7° and 45°.

The basic composition of TSV is apparent from the energy spectrum. The vast majority of the characteristic peaks are K-transitions with a few being of L-origin. The raised baseline is caused by the noise, especially containing bremsstrahlung. Individual height steps in the background are caused by bremsstrahlung absorption and following secondary fluorescence generation.

The metallization of the core is formed of Cu atoms and their compounds. The protective layers consist of a silicon oxide barrier. Additionally, weak titanium and nitrogen peaks of the diffusion layer could also be observed in several configurations. On average, the chemical signals were shown to have regular distributions. At the moment, no significant correlation of chemical composition and TSV malfunctioning was found. Information depth of EDS estimated by Castaing's formula is ∼1.35 µm for silicon. Thus a more surface-sensitive method is needed. The EDS mapping results, however, provide a significant tool for the correlational image fusion shown in Section 5.2.

AFM topography

Atomic force microscopy is a *scanning probe microscopy (SPM)* technique of imaging a sample with a microscopic probe scanning the surface of the studied area [57]. The probe consists of a sharp tip located at the end of a flexible cantilever or quartz fork. As the distance of the tip from a surface is less than 100 nm [58], it experiences attraction and repulsive forces. Tip-surface interactions are evaluated at each point to create a 3D topographical map.

LiteScope is an AFM instrument with a selfsensing probe designed for operation in an electron microscope chamber. Using its CPEM technology - correlative probe and electron microscopy - AFM and SEM measurements can then be performed simultaneously at the same sample location. This experiment was performed in collaboration with NenoVision company, the developer of LiteScope devices.

Since the ROI was milled down with the 45° angle, it is necessary to correct its spatial orientation suitable for AFM. A sample holder for the silicon wafer with glued TSV was 3D printed to properly orient the plane for AFM tip.

Litescope AFM provides correlative imaging of the cross-section topography using the signal of SE, BSE, and AFM cantilever deflection. Areas were selected for the research of step-height abnormalities of individual inner layers of TSV, in spite of charging, which complicated the measurement. This effect is most noticeable in Figure 4.10. Red arrow indicates the topography region of detected pore or a hole in the copper layer, as predicted by high-resolution CT data in Figure 4.2. Thus confirming Cu layer is not void-free.

Other areas showed an interlayer step-height of up to 600 nm. EDS point spectrum of an interface determined presence of Si, Cu, and O atoms. This uneven surface is probably caused by some structures growing during sample storing.

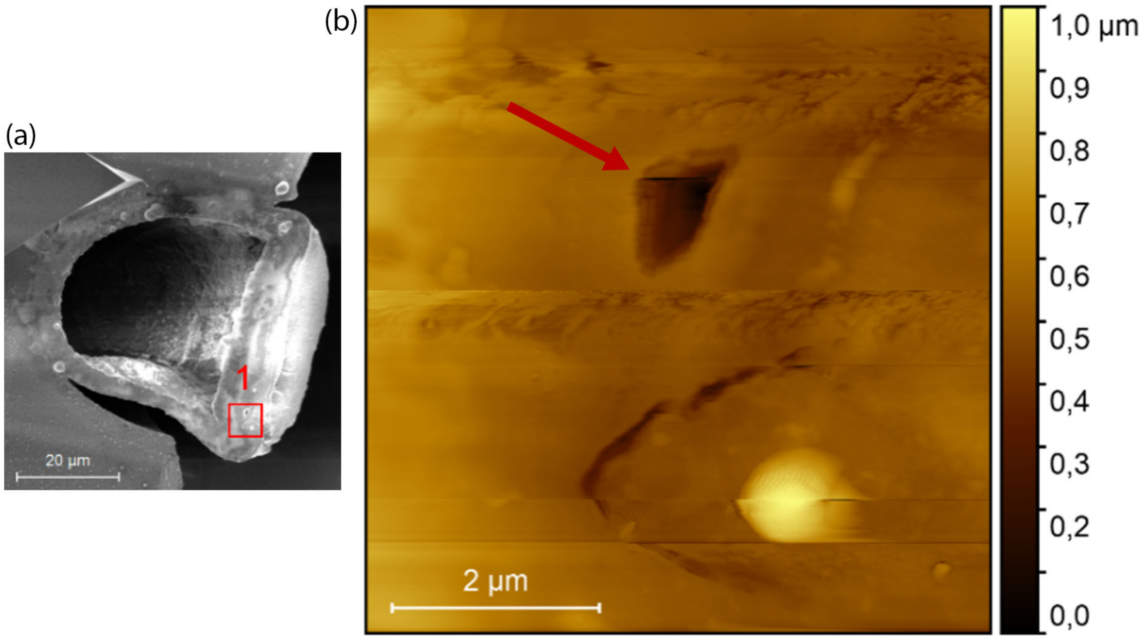

Figure 4.10: TSV sample 9 section topography. (a) ROI marked with red square, (b) topography of the surface with marked hole area. Fluctuations are caused by sample charging.

FIB-SEM 3D tomography

After the thorough TOF-SIMS study of cross-sections (Subsection 4.3.3), to investigate the subsurface development of the TSV sample 9, FIB tomography was adapted. Apart from SE detection, EDS spectral mapping was additionally acquired at every 3 slices for time efficiency. Automatic measurement by internal Helios software *Slice&View* helps with the FIB step movement and image saving. The cycle goes as followed. Data collection is initiated at the first cross-section by obtaining SE image with EDS spectral map included. The milling box (Figure 4.6b) mills down a defined slice thickness (in this case 300 nm) and depth. The 30 µm milling depth has been tested sufficiently for the TSV sample 9 size with 21 nA beam current, even though the dimensions are greater. After each cycle is complete, the system re-positioning is achieved by a two-step process of stage and beam shift according to the fiducial markers. A total of 158 images was collected with measurement time of 15 hours.

SE images were firstly stripped of debris after milling. Selected slices, which suffered from curtaining effects, were adjusted according to the process described in Section 5.1.2. Afterwards, both SE and EDS images were aligned. Different approaches were tested, the combination of *gravity centers* with disabled rotation followed by *least square method* in Avizo worked best (for additional alignment tools see Section 5.2). Nonetheless, human correction was still needed for some slices.

3D reconstruction of SE images did not contribute to any interesting output. On the contrary, after examination of each section (Figure 4.11a), the bubble development was pointed out. The single most striking observation to emerge from the data comparison of EDS (Figure 4.11b) and SE was the passivation layer adhesion to the other layers. From the spectral images, it is clear that the SiO_2 protective layer is in fact attached to the silicium wafer and only the copper core forms the bubble (Figure 4.11d). Thus, PVD of the Cu seed layer has failed in the sample 9.

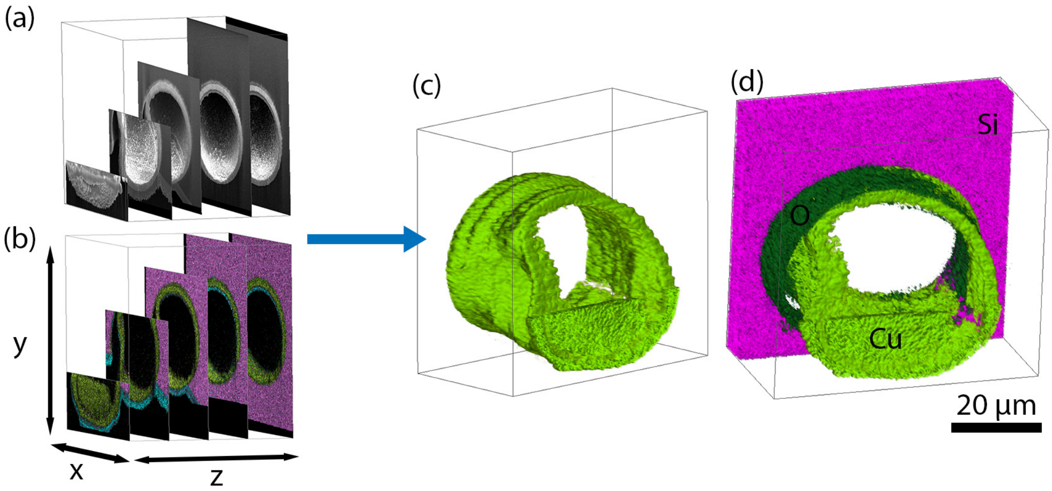

Figure 4.11: The procedure of FIB-SEM 3D reconstruction of the TSV sample 9. Stack of (a) SE and (b) overlaid EDS images, (c) 3D reconstruction of Cu spectral maps, (d) 3D reconstruction of Cu, O, and Si maps. Copper layer deformation and detachment is distinct.

4.3 FIB-SIMS

Unlike EDS, where the interaction volume is in the range of a few micrometers, SIMS demonstrates spectacular surface sensitivity and comparable spatial resolution. Nowadays, it is becoming more popular to implement mass spectrometers into dual-beam systems and thus utilize the unique properties of the focused ion beam. McPhail et al. (2008) [59] conducted a series of experiments with this setup. However, the ppb sensitivity and mass resolution can only be achieved with dedicated SIMS devices. The measurements in this work were performed on TOF-SIMS5 instrument in CEITEC. Primary ion beam (internally called LMIG) consists of Bi_{1-7}^+ ions. Secondary sources are Cs^+ or O_2^+ ion guns for depth profiling and secondary ion yield increase, Ga^+ focused ion beam and Ar^+ or O_2^+ cluster ion sources which are used for crater and wedge preparation.

FIB-SIMS is a novel technique with interesting advantages involving the high sensitivity of SIMS method in combination with precise serial sectioning by FIB. During the last 5 years, this method has been promoted mainly in areas where traditional depth profiling lags behind. These are very deep craters, or materials with different sputtering rates or porous structures. In comparison, FIB-TOF-SIMS conserves the relative depth position of different chemical constituents and keeps the high lateral resolution of ∼100 nm. Additionally, for depth profiling by Cs^+ or O_2^+ ion guns 180° apart from LMIG, observing any lateral interlayer diffusion in the TSV is limited by the geometry, as the profiles would be aligned within the plane of each successive image with inferior resolution.

A recent study by Barnes et al. (2016) [60] involved one of the first 3D TOF-SIMS studies of TSV. It was confirmed that the limitation of FIB-SIMS technique is the secondary ion yield, depending on the ionization probability of species and the sample geometry[5].

4.3.1 TOF-SIMS5 tomography geometry

Since the previously mentioned ion sources are aimed at the sample at an angle of 45° and are turned 90° from each other, a few options for tomographic analysis arise. The initial V-shaped trench milled down by FIB creates two possible areas for LMIG sputtering, a 45° plane and a 90° plane. All prior experiments [11, 61] have established workflows at the 45° plane. It allows the application of all three ion beams - primary ions of Bi^+ for analysis, FIB for sectioning, and O_2^+ ions to remove residual parasitic gallium and to increase the secondary ion yield. The disadvantages, unfortunately, are the oblique sections and thus deformed secondary ion images due to the LMIG position. This image deformation must be compensated during the computer reconstruction of individual slices. Furthermore, the side wall trench shields the part of the cross-section and prevents a homogeneous dose of oxygen ions.

The 90° plane is suitable for LMIG sputtering, as the structure is perpendicular and there are no side effects due to the ion column geometry. However, this area is completely hidden from the oxygen ion source. It is therefore impossible to remove residual gallium after each tomographic slice. The yield itself can be increased by flooding oxygen atmosphere in the microscope chamber at a pressure of the order of 10^{-6} mbar. Nevertheless, the results do not show a striking increase. There is the possibility of stage rotation to access the 90° plane by O_2^+ ion source at one position and by FIB+LMIG at the other. This is discussed in following Subsection 4.3.2.

---

[5] This is frequently the most significant issue during any tomography measurement.

4.3.2 SIMS rotary table adjustment

Since the whole tomographic measurement is a very time-consuming experiment (in the order of several hours up to days) and is not sufficiently automated within the Iontof software, the external script was developed using the AutoIt program. The first automated procedure was performed by the author of the thesis after completing the bachelor's degree. Subsequently, there was a significant improvement of the script by including the implementation of the formerly mentioned sputtering gun at each tomographic cycle [61].

Conventional tomography consists of dozens of cycles. To involve the stage rotation in the automation, the deviation during each rotation step must be taken into account. This would call for an accuracy of tens or hundreds of nanometers during each rotation. If the inaccuracy was greater, it could happen that after a few cycles the ROI disappears from the field of view and the cutting will be inaccurate.

TOF-SIMS5 sample holder

The rotation of the whole sample holder in TOF-SIMS5 was tested. In the case of eucentric rotation, the deviation was around 20 µm per cycle. In the case of rotation, when the ROI was in the axis of rotation, the inaccuracy dropped to 17 µm per one cycle. If the deviations were steered in a certain direction, it would be possible to adjust either the raster of ions or stage movement. However, after some time, we came to conclusion that the divergences were completely randomized. Such shift would be unacceptable in long-term automated measurement. Human corrections after each cycle would be required.

Rotary table adjustment

Another considered option was a sample holder developed by former BUT[6] student Juraj Karlovský. As part of his master's thesis [62], he modified and assembled a sample holder in order to tilt the samples vertically. His solution is suitable for the mounting system in the TOF-SIMS5 microscope and is UHV compatible. The mechanical movement is provided by a linear piezoelectric motor from SmarAct company [63]. A system of pulleys and an endless ⌀0.1 mm tungsten wire was adapted to create a rotation in the x-axis. We tried to modify this concept by converting the linear shift of the piezo motor to a rotary horizontal displacement.

The original design includes a pulley for redirecting the wire at a 90° angle. This area could be used so that the friction of the rope movement rotates the pulley sufficiently. If a sample is placed on the rotary axis, theoretically, it would be able to rotate with precise steps of the linear piezo motor movement.

---

[6] Brno University of Technology.

The simplicity of the movement of the pulley is ensured by steel bearings. Purchased bearings are with the highest possible accuracy (the smallest internal clearance offered by the manufacturer) and compatible with UHV environments with dimensions $d = 4\,\mathrm{mm}; D = 9\,\mathrm{mm}; t = 4\,\mathrm{mm}$. Bearings were placed on the newly designed pivot (Figure 4.12), which is attached to the sample holder at the bottom with 4 M2 × 8 screws. The lower pulley was slightly improved from the original design by decreasing the clearance between the bearing and increasing the groove for the wire turn in the lower part of the holder.

The upper pulley has been freshly devised (see Figure 4.12). It houses two bearings for maximum clearance limitation. The cover part is formed with a closed lid to fit samples up to 14 mm in diameter. A deep groove is included for the wire for better traction. To prevent contact between the bearings, spacer rings were manufactured to keep them at a constant distance.

Since the piezoelectric motor does not have the possibility to read its relative position, the pulley movement has to be limited between only two positions. These specific positions correspond to the sample rotation, where the 90° plane is accessible by both LMIG + FIB and the sputter gun. This was solved by a stationary barrier, by which the rotation of the pulley would stop and bounce between the back and forth positions.

Each part was made from aluminum EN AW 6061 for its better availability and machinability. I would like to thank Dominik Varga from CEITEC facility for the manufacturing of the designed components.

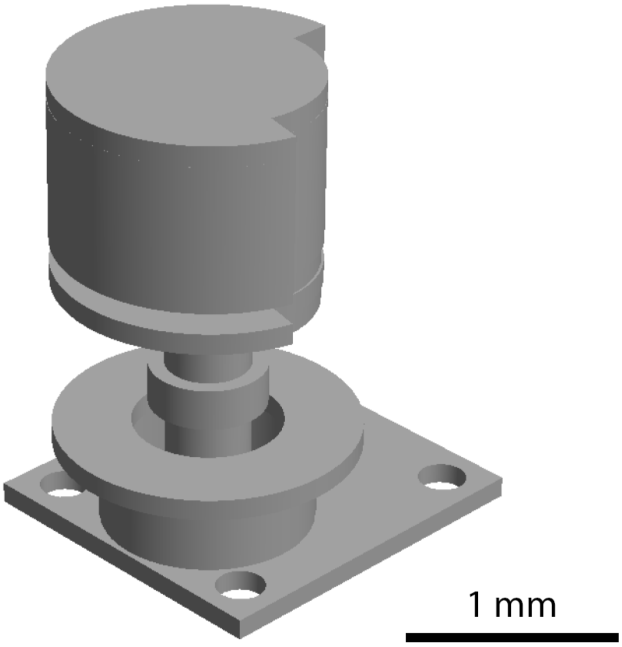

Figure 4.12: Pulley system model for the 90° sample rotation implemented within the original design of the sample holder by Juraj Karlovský [62].

Rotary table testing

During the first experiments, the inclination of the sample was noticeable in both stopping positions. The reason is probably caused by the tension of the wire on the inside of the groove in the bearing cover. This phenomenon was reduced by inserting a stable barrier between the grooves. Other attempts to limit staggering, which plays a substantial role in the uncertainty of individual cycles, have involved minimizing the clearance of individual assembled components. A punch (tool)[7], foil, and sheet metal were used to compensate for the wobble of the bearing cover, on which the specimen is placed.

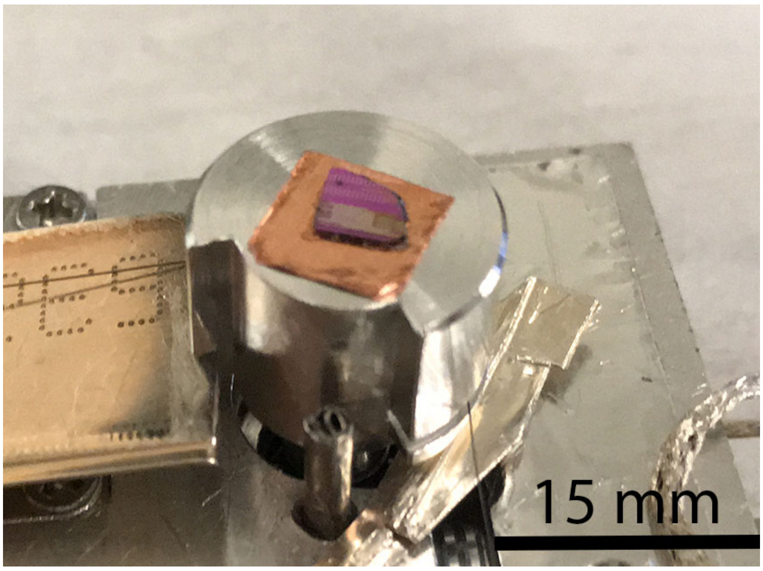

Figure 4.13: View of the adjusted TOF-SIMS5 sample holder for horizontal piezo rotation.

The resulting SIMS sample holder is shown in Figure 4.13. After a series of conducted experiments, we were able to reduce the uncertainty up to $(1.2 \pm 0.5)\,\mu\text{m}$ during each rotation. Overall, these results indicate remarkable improvements by at least one order of magnitude from the original SIMS sample holder. Several tomographic cycles can be performed successfully at the 90° plane with the implemented sample rotation and thus reduce the bismuth secondary ion image deformation. However, to fully automate this process, more accurate sample rotation would be necessary.

What is interesting that this experiment of back and forth rotation has been also tested with a rotational piezoelectric motor from SmarAct company built into a sample holder developed by TESCAN company. After the conducted evaluation, we detected the uncertainty of this device ranging from 0.8 µm to 1.5 µm. Both sample holders reported similar deviations, which unfortunately do not reach the accuracy necessary to automate FIB-SIMS tomographic measurements lasting 24 h or more.

4.3.3 Sample 9 FIB-SIMS

FIB-SIMS measurements can be conducted immediately after the sample preparation (Subsection 4.2.2). The focused ion beam sections were made at a 45° angle on TSV sample 9. During the milling, the cross-section was analyzed at different depths adjacent to the bubble defect (two of those are demonstrated below). Ion pulses from LMIG in the form of Bi_1^+ or Bi_3^+ primary ions with an energy of 30 keV were targeted at the surface. The fastimaging mode of the mass filter was favored due to the increased lateral resolution. To rule out the possibility of missing any element's trace amounts, both positive and negative polarization of SI was tested out. The most prominent results were achieved by positive SI detection with either oxygen flooding or O_2^+ ions bombardment. The oxygen partial pressure of 5×10^{-6} mbar was introduced in the analysis chamber. 2 keV O_2^+ ion sputtering with 600 nA beam current although removes a couple of atomic monolayers from the surface, but increases its matrix effect properties and thus SI yield.

---

[7] V češtině důlčík.

The length of each ion beam cycle was set to 45 µs, which corresponds to the mass range of 1–185u. Longer time and thus the ability to detect heavier atoms would be pointless, as the composition according to the manufacturer consists of elements ≤ 70 u. Delayed analyzer extraction was adopted to help with the time-of-flight compensation for ion energy spread and improve mass resolution. Cross-section analysis consists of 278 scans in 8 h time period.

The first cross-section results are presented in Figure 4.14. The data obtained by ToF-SIMS confirm and supplement the results by EDS. Figure 4.14a shows the analyzed area by SE detection. Cu grains can be observed in the metallization layer. Figure 4.14b - 4.14e identify the regular composition of TSV sample 9: isotopes of ^{63}Cu and ^{65}Cu, TiN, Al, SiO_2 barrier layers. RGB overlay of Cu (red), Al (green), Ti (blue) is illustrated in Figure 4.14f.

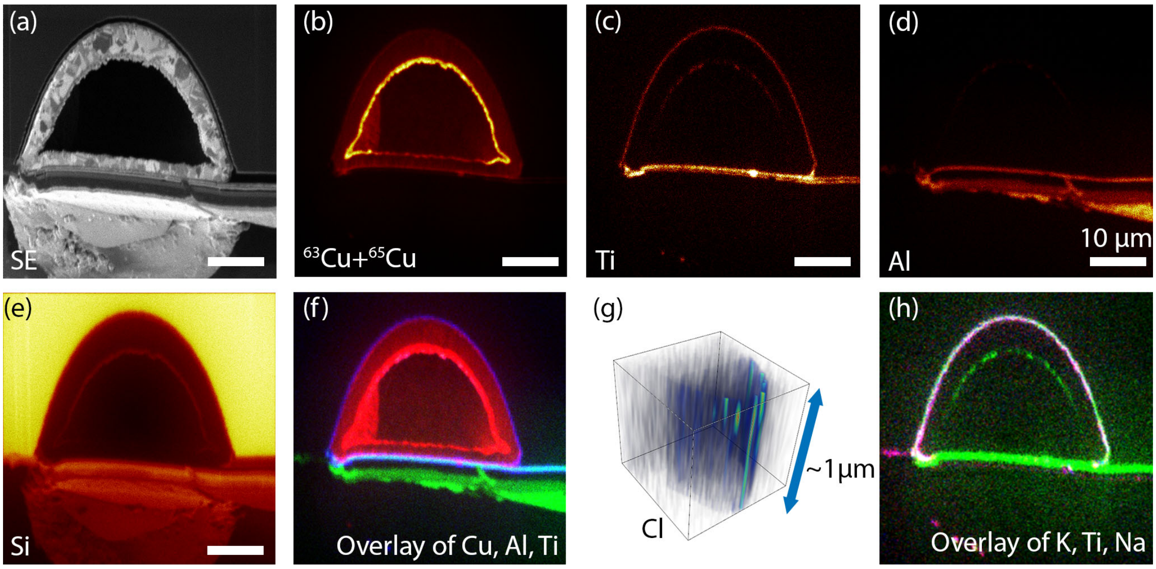

Figure 4.14: TOF-SIMS results of the first TSV sample 9 cross-section. (a) SE image created by impinging Bi^+ ions, signal of (b) Cu isotopes, (c) Ti, (d) Al, (e) Si, (f) RGB overlay of Cu (red). Al (green) and Ti (blue). (g) represents Cl distribution resulting from depth profiling, (h) overlay of Ti (green), K (purple), and Na (white) signal. Graphic scale on all spectral images is 10 µm.

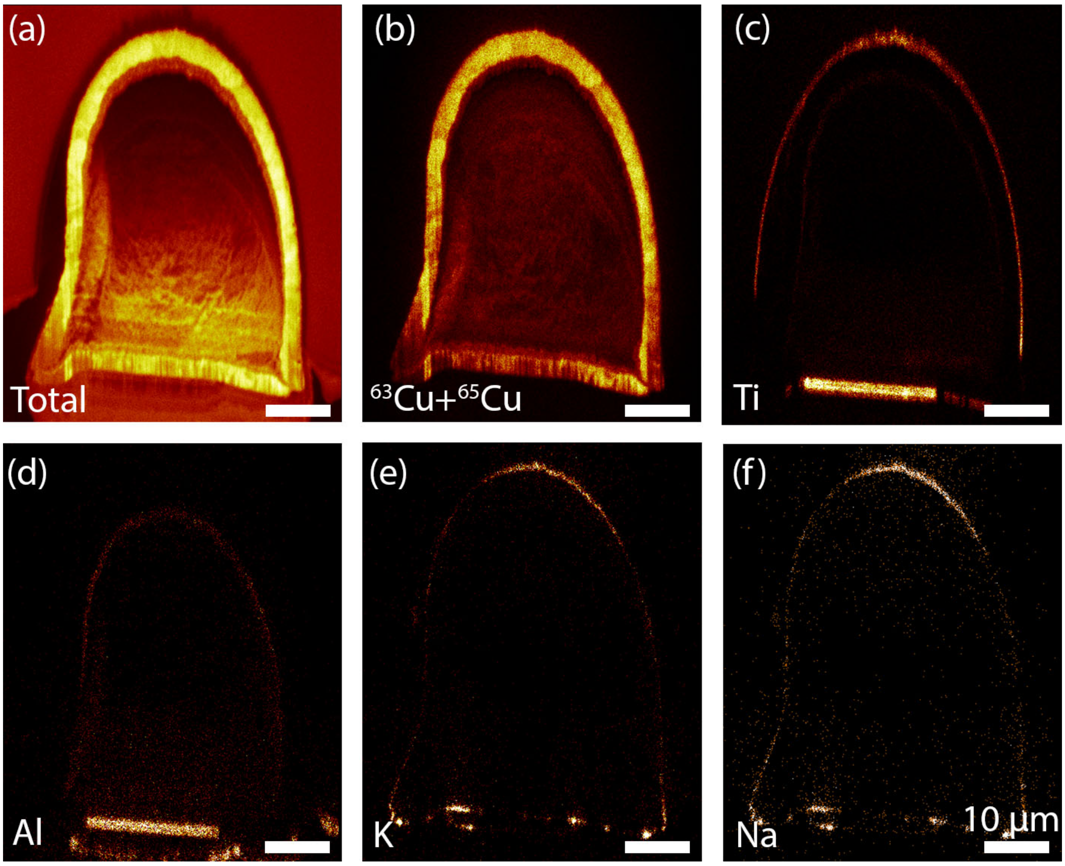

Figure 4.15: Secondary ion signal of the same cross-section as in Figure 4.8c. (a) is the total detected signal, (b) Cu isotopes, (c) Ti barrier, (d) Al, (e) K , (f) Na ions. Graphic scale on lateral images is 10 µm.

What is new from the EDS characterization, strong evidence of contamination was found when mass peaks of Ca, K, C, S, Cl, Na were detected in the cross-section. Figures 4.14g and 4.14h represent the examples of two abnormal elements. Contamination of Cl was observed mainly in the region of the Cu signal origin. After measuring a shallow 1 µm depth profile (Figure 4.14g) in the dynamic SIMS mode, we discovered an inhomogeneous chlorine distribution. The last Figure 4.14h shows the overlay of Ti(green), K (purple), and Na (white). What is interesting about the data, that the potassium and sodium is present within the known TiN barrier layer at the CuTiN and TiNSiO$_2$ interface.

Figure 4.15 corresponds to the cross-section depth in Figure 4.8c. SIMS confirms the regular distribution of inner layers without distinct deformation. However, as in the previous cut, some precipitates of K and Na ions are detectable in the Ti layer. A possible reason of the presence of the contamination is the Fraunhofer IKTS cleaning process. During a preparation of the CT analysis, a cleaning liquid is introduced to the TSV. The samples are purified using distilled water, acetone, and ethanol. These solutions might intertwine into the pores and joints of the TSV and the remnants are bounded to Cu.

Furthermore, the interface between Ti, SiO$_2$ and Si layer is without any distinct space or pores. This observation may support the hypothesis that the deposition of metallization has failed, thus creating a poor step-coverage of only the Cu in the bubble region.

FIB-SIMS 3D tomography

Since FIB tomography is a destructive technique, it is not possible to analyze the same area of TSV as in the case of Figure 4.11. The FIB-SIMS 3D study therefore continues in the intact region, where the original measurement was interrupted.

The experiment geometry was selected as follows. The FIB sectioning maintained the 45° milling plane due to the TSV on wafer placement. However, to improve the bismuth imaging side effects of distorted structures owing to TOF-SIMS5 ion source arrangement, the first tomographic measurement with the stage rotation was attempted. The two stage positions of 90° apart were fixed: FIB milling and LMIG analysis with oxygen sputtering. Unfortunately, as the automation of SIMS rotation is questionable at this time, human corrections had to be made during each tomographic cycle.

Achieving the required outgoing secondary ion signal turned out to be a key parameter of the measurement. A sufficient dose to interpret lower-concentration contamination of the TSV is $> 5 \times 10^4$ particles of a single compound per one image. Several procedures were adapted to increase the sputter yield: partial oxygen pressure in the main chamber, homogeneous O_2^+ sputtering after each gallium sectioning, 5° stage tilt towards the LMIG and finally a relatively long Bi_1^+ analysis of the cross-section (50 min). Additionally, since the TSV core itself is covered under a layer of ≈60 µm of silicon, FIB sectioning stretched for 20 min each. All these experiment modifications culminated in a total measurement time of ∼28.5 h. With respect to time savings, the total number of sections was reduced to 20 and with 1 µm step size.

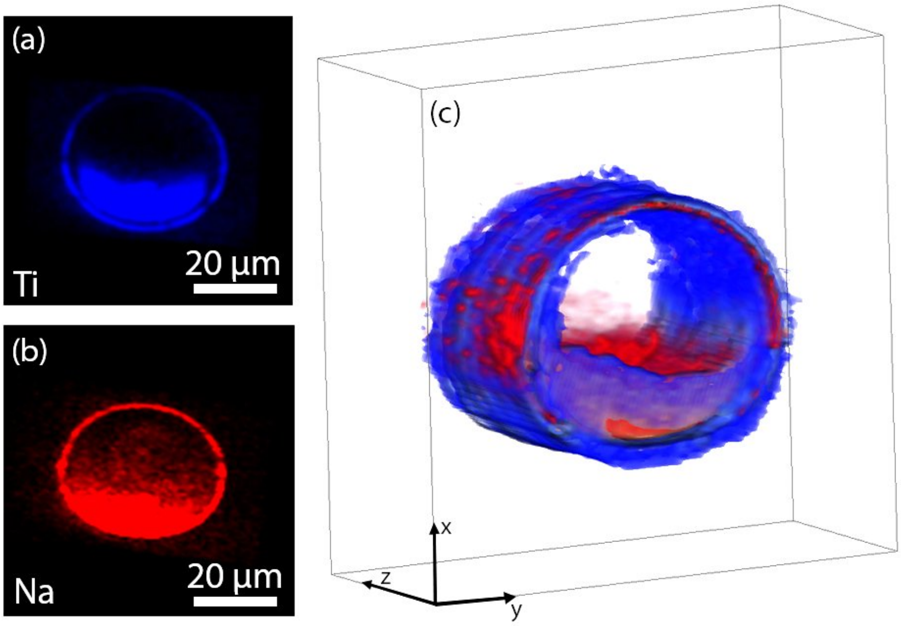

Figure 4.16: Presented tomography image of titanium layer (a) and its sodium contamination (b) in TSV sample 9. (c) Computer 3D registration of the two signal overlay.

The purpose of FIB-SIMS tomography was to confirm the presence of unwanted elements throughout the entire TSV sample 9. Its distribution did not differ noticeably from neither Figure 4.14 nor Figure 4.15. Thus we can exclude the correlation between contamination and the large bubble at the front side. As an example of possible data interpretation, we mention Figure 4.16. A 3D computer rendering of aligned Ti^+ and Na^+ images was performed in Avizo. The greatest focus was on image filtering and thresholding so that even such a small number of slices resulted in a continuous shape. On average, sodium was uninterruptedly present in the whole TiN layer. This concludes the relationship between contamination and bubble. These two irregularities are not connected.

5 DATA CORRELATION

The connection of several techniques has found application in semiconductor failure analysis. Correlative measurements allow to gradually plan the workflow and obtain complementing results from each technique. Part of the Cool_PROMO project is the data processing to comprehensibly present the acquired information to the TSV manufacturers in order for them to be able to further eliminate the error rate of their products. One of the reliable and established techniques of presenting correlative imaging modalities is the so-called *image fusion*. It is a combination of multimodal images into one more intelligible output.

This chapter gives a brief overview of the theoretical foundations of image processing (Section 5.1), outlines the procedures of reduction of shortcomings during FIB tomography (Subsection 5.1.2), and discusses two methods of image fusion and subsequent presentation of the obtained data (Section 5.2).

5.1 Image processing

This section serves as an explanation to the digital image processing of the results obtained in this thesis. A digital image is defined [64] as two-dimensional function, $f(x,y)$, where x and y are position coordinates in the matrix of numbers, and the amplitude of f is the intensity of the image at a certain point. A pixel is a finite element of an image with a particular location and value. The value of intensity level is typically an integer power of 2, meaning the size S of an image with M columns and N rows is calculated as $S = M \times N \times 2^k$, where k represents a k-bit image. For instance, the 256 discrete intensity value image has a depth of 8 bits.

To evaluate the obtained data, one must work with the image to enhance the features of interest. Processing the image for visual interpretation severely depends on the human perception of the modified details, as such not all adjustments are considered an improvement by some individuals. We will, however, try to perform any of the manipulations with care.

5.1.1 Image filtering

The simplest operation on a digital image is the alternation of the values or coordinates of individual pixels, thus in the spatial domain. *Averaging* is a transformation of a pixel value based on its intensity at the (x_0,y_0) position by computing the average of pixel values in its neighbourhood $m \times n$. The coordinates transformation is defined as [64]

$$(x,y) = T(x_0,y_0), \tag{5.1}$$

where T is the matrix of transformations such as scaling, rotation, translation, and shearing. For merging two images, it is convenient to scale both input images to the same size. A series of affine transformations were used to align subsequent images.

Spatial filtering is a process of operation on the pixel and its neighbourhood. The image response $g(x,y)$ of a filter is the sum of a series of filter coefficients applied at each pixel of the mask size $m \times n$. Such filters can help in noise reduction, for example, the median filter. As the name implies, the value of a pixel is replaced by the median of its neighbourhood pixel intensity. Spacial filtering becomes handy in the processing of secondary electron images [65] for detail enhancement, smoothing[1], sharpening to increase contrast and accentuate detail, noise reduction, and background removal[2] to correct an uneven illuminated background.

5.1.2 Frequency domain

Since Jean Baptiste Fourier stated that any periodic function, and even nonperiodic functions with finite area under a curve, can be expressed by the sum of sines and cosines with different frequencies and multiplication coefficients, Fourier series and Fourier transform became a fundamental tool in mathematical operations and digital image processing later on [64]:

$$F(u,v) = \int_{-\infty}^{\infty} \int_{-\infty}^{\infty} f(x,y) \exp\{-i2\pi(ux + vy)\} \, dx \, dy, \tag{5.2}$$

where $F(u,v)$ represents the Fourier transform of original function $f(x,y)$, x,y are referred to as spatial domain variables and u,v the frequency variables.

The main advantage is the possibility of switching the domain of a function without a loss of any information. Direct associations between an image and its transform are hardly recognizable, although there are some correlations within the intensity variations. As such, since the frequency is related to the rate of change, the lowest frequencies ($u = 0, v = 0$) are proportional to the slowly varying intensity changes (illuminance, shape, orientation) and as we move away from the origin of the transform, the higher frequencies are local features of an image and correspond to abrupt changes in the image (edges, fine details).

This knowledge of frequency-intensity correlation was used for *lowpass* and *highpass* image filtering, which allows the passing of low or high frequencies to blur or enhance sharp details (Subsection 5.2.2) before carrying out an inverse Fourier transform to obtain a filtered real-space image. Another notable example of Fourier filtering is applying a certain frequency bandpass filter for specific sizes of a feature in an image to select its minimum and maximum size. This distinction can be further beneficial during subsequent global thresholding of SE images.

---

[1] This filter replaces pixel value with the average of its 3×3 neighbourhood.

[2] Based on the rolling ball algorithm. A local background value is determined for every pixel by averaging the pixel values within a paraboloid. This value is eventually subtracted from the original image.

Additionally, by applying Gaussian filter function to the 3D reconstruction, a slight blur is introduced that can compensate for a discrete amount of tomographic images, thus creating a continuous impression without gaps between slides.

Curtaining removal

Curtaining aka waterfall effect is one of the most common and visible FIB artifacts. Milled face exhibits parallel scratches in the ion beam direction (usually vertical). This implies that more or less material was removed. It is due to the sputter yield dependence on the incident beam angle. At higher incident angle, the collision cascade is located directly beneath the surface and more near-surface atoms receive enough energy to get sputtered [27, 66]. These locally enhanced angle differences are caused by an irregular or non-flat surface, such as porosity, grains of heavier elements, or surface structures.

Curtain-removal methods are either image post-processing or adjustment of measurement parameters, such as the protective layer deposition or a lower beam current. An advanced technique developed by TESCAN company [67] is a piezo motor stage for additional cross-section tilt. During the FIB milling, the tilt change establishes artifacts in different directions and then polishes at the original tilt before curtaining reappears.

The literature on FIB curtaining removal has highlighted several approaches. The most prominent results were proposed by Liu et al. (2018) [66]. We attempted to replicate this method on the most curtain-affected FIB sections (Figure 5.1). The principle is in the Fourier filtering of the affected parts of an image. In the original image $f(x,y)$ (Figure 5.1a), the curtaining effect is vertical (nearly parallel) scratches. After conducting 2D Fourier analysis on $f(x,y)$, the curtaining effect is presented as horizontal stripes. At first, a part of f(x,y) with similar curtaining intensity is cropped out. After FT, a band around the curtaining frequencies is enveloped to create a notch filter. If the inverse FT image g'(x,y) demonstrates curtain-free area, the notch filter can be applied to the original image, followed by grey-scale thresholding to adjust the overcorrected areas.

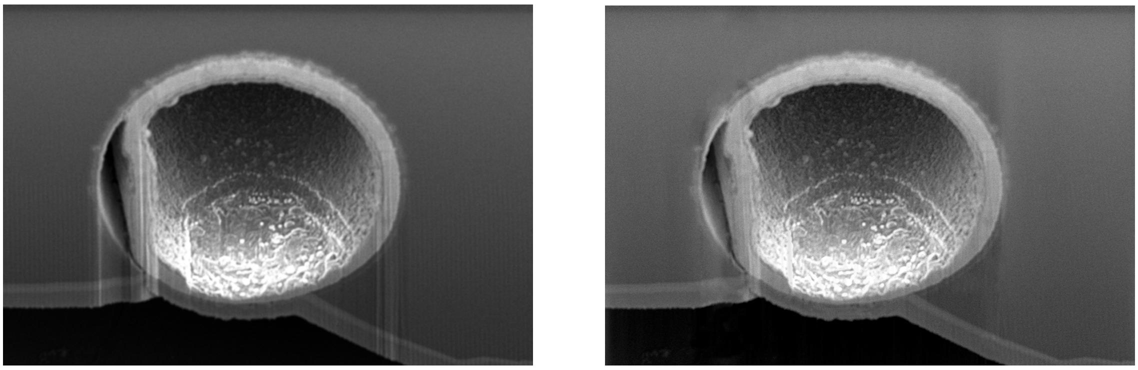

(a) Original image. (b) Processed image.

Figure 5.1: Example of the curtaining removal technique on a TSV cross-section. The output image is stripped of the main scratches, although an artefact in the form of slight contrast differences emerged.

A clear benefit of this technique is in the removal of the majority curtaining artifacts, however possibly the most diverse scratches persists. Some regions might also exhibit different brightness and contrast levels.

5.2 Image fusion

Image fusion is a term to describe the post-processing of retrieving important data from a set of images and combining them into a single more complex and informative output image. Nowadays, image fusion is being used in fields from medical diagnostic images, geographical topography, to motion control of smart robots [68].

In the simplest case, two images visualizing the same area are overlaid in software, for instance, spacial domain techniques such as average, minimum/maximum pixel value, or block replace, nonetheless frequently introduce noise. One of the preferred and straightforward fusion techniques is alpha channel blending. A transparency channel image with values from 0 denoting completely transparent image to a value of 255 denoting a completely opaque image is introduced to the blended background image.

While processing electron microscopy and spectroscopy images, the effects of different contrast mechanisms, resolution varying by orders of magnitude, and chosen color space must be considered to avoid misleading artifacts. More advanced methods like the IHS color space transformation, and pyramid-based fusion are attempted in this thesis.

Images introduced into the fusion algorithm are firstly preprocessed. Softwares such as Fiji ImageJ, Avizo, and MATLAB were adapted for image manipulation. When merging two images, its alignment (rigid, shear transformation), i.e., carrying out the coordinate rotation, translation, and/or scaling transformation plays an essential role, hence any misalignment would be significantly projected into the final result. The hierarchical strategy is employed, starting with a coarse resampling of the data set, and proceeding to finer detail matching later on. Many registration tools were adopted: ImageJ plugins: *TrakEM2* [69], *StackReg* [70], *Turboreg* [70], *DS4H Image Alignment* [71], *SIFT Stack Linear Alignment* [72], *Virtual Stack Registration* [73]; Avizo align function [52] with *gravity center* or *least square method*. Unfortunately, none of the previously listed tools is universal and need to be adjusted or manually corrected according to the specific images.

Figure 5.2 illustrates the correlative 2D microscopy and tomography results. In this case, XCT slices of TSV sample 9 from Fraunhofer IKTS after its 3D reconstruction were adjusted to match the dimensions of the actual device. The angle of the real FIB cut was meant to be in the 45° direction, however, the TSV could have been misplaced on the Si wafer and slightly tilted due to the glue underneath. We determined this cross-section plane angle by comparison of SEM images of the TSV and XCT model. The plane coordinates were imported to the Avizo software, thus the visualization of the Cu SIMS detection could have been presented (Figure 5.2a). Cu map appears to be marginally misaligned. The reason for that lies in the true coordinates of the plane, but also in the SIMS sputtering of the cross-section. Multiple measurements were performed on the cross-section, thus its resemblance could have been changed.

Figure 5.2b provides the correlative tomography overview of the sample 9. The XCT data were stripped of surrounding and inner voxels to resemble the Cu core of the TSV and EDS spectral images containing O maps were aligned and assembled into the 3D model. Registration of two 3D images was executed in Avizo software using *Register Images* plugin. At first, the coarse matching is done by computing the centers of gravity considering the voxel values of both data sets as weights. A slight shift still remained. More refine registration is achieved by principle axis alignment. The resulting image shows a 3D form of the TSV core, including the edge insulation barrier made of SiO_2. As mentioned in connection with Figure 4.11, the bubble defect is caused by the failed adhesion of the metallization layer. This 3D model confirms this.

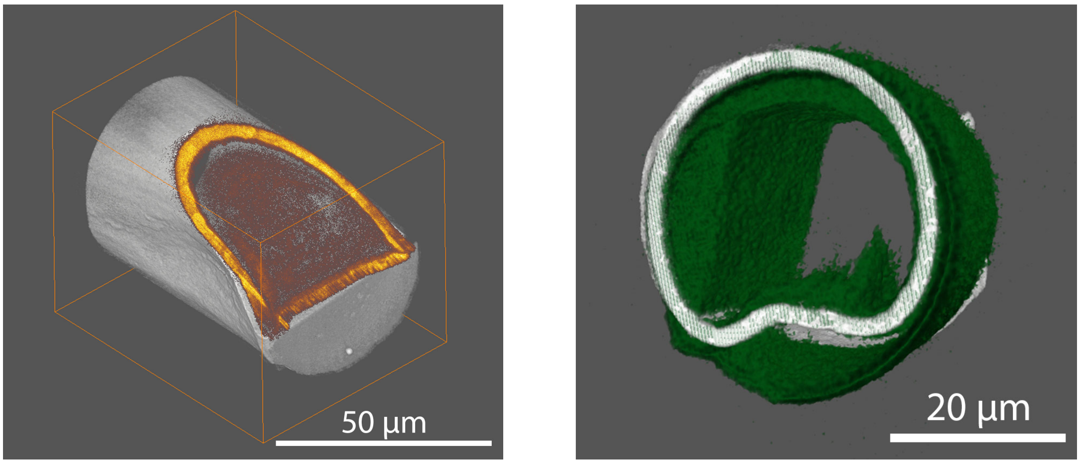

(a) CT data with Cu signal.

(b) CT data with O signal.

Figure 5.2: Examples of results correlation. (a) CT data of sample 9 overlaid by Cu signal from SIMS cross-section measurement. (b) CT data of sample 9 overlaid by O 3D model created by FIB-SEM (EDS) tomography of part of the TSV.

5.2.1 Intensity-Hue-Saturation fusion method

Images processed in this thesis are partially grey-scale, however, the spectral maps of EDS or SIMS are colored based on the elements present. Apart from the standard RGB color model, where each point is represented as a combination of primary colors, red (R), green (G), and blue (B), therefore in a case of 8-bit image, the pixel depth is 24 bits[3], light can also be described via distinguishing one color from another by *intensity, hue, and saturation* (IHS) [64]. The graphic explanation provides Figure 5.3. Intensity in this color model represents achromatic notion of brightness, hue is the aspect of the dominant wavelength, which is perceived by an observer, and saturation is associated with the purity or the amount of white color within the hue attribute [74]. In essence, the intensity channel is assumed to carry mostly structural information, while the saturation and hue channels contain spectral information, i.e., color. The advantages of IHS system over the RGB are the aspects of an image that are easily identifiable by distinct color attributes, meaning any colors apart from the primary RGB might not be displayed by uniform color gradation. Additionally, there is an option for decoupling the color and gray scale information, thus it is convenient for image fusion of colored and colorless images [75].

---

[3] This creates 16 million color options.

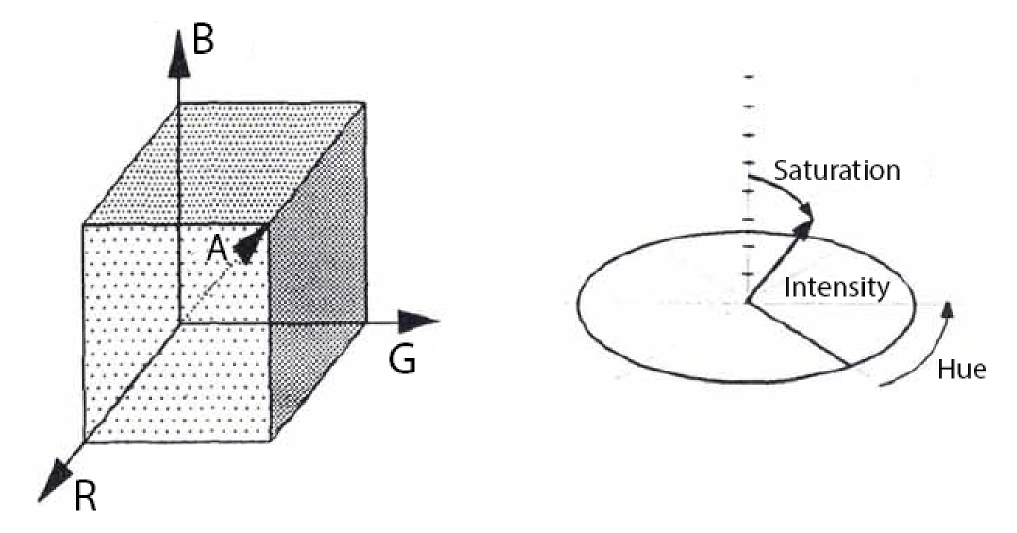

(a) RGB color space. (b) IHS color space.

Figure 5.3: Graphic representation of color spaces. (a) Cartesian RGB space with red, green, and blue axes defining the x,y, and z vectors. Vector A describes the grey vector with the end in black. (b) Intensity representing total energy of the image is displayed as radius of the sphere. Hue, as the wavelength, is circumferential angle. Saturation is the percentage of white light in the image and is shown as polar angle in the spherical coordinate system. Adapted from [75].

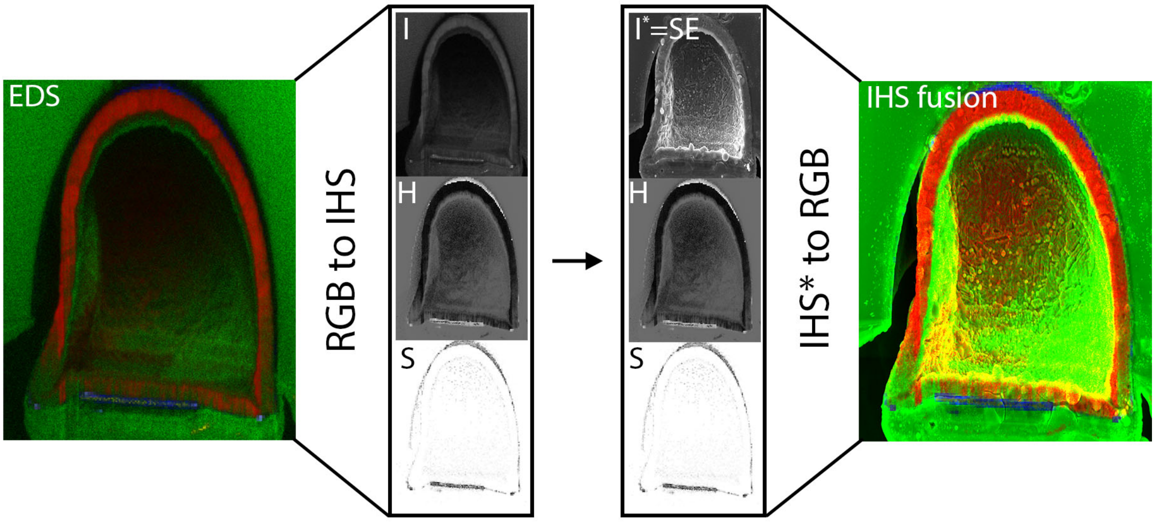

Figure 5.4: Intensity-Hue-Saturation image fusion method. Representation of high-resolution SEM image of the sample 9 cross-section merged with SIMS data. In the IHS sharpening, the intensity channel of SIMS image is replaced by the SE image.

After the image registration, low-resolution spectral image is scaled to the same size of the grey-scale SE image of the same ROI. The SIMS/EDS image in 24-bit RGB color space is transformed into the IHS model (Figure 5.4). What follows is the replacement of a spectral intensity channel by a grey-scale SE image. Hue and saturation are merged with the new intensity channel and transformed back to the RGB [68]. The pixel values of the fused image $g(x,y)$ are a function of both inputs combined [74]:

$$g(x,y) = f(i_1(x,y),i_2(x,y)). \tag{5.3}$$

The IHS fusion algorithm is a straightforward technique. Both Fiji ImageJ processes and a MATLAB script were implemented to quickly fuse any given two images. Such examples of possible abrupt IHS fusion are FIB-SEM (EDS) tomography slices (Figure 5.5).

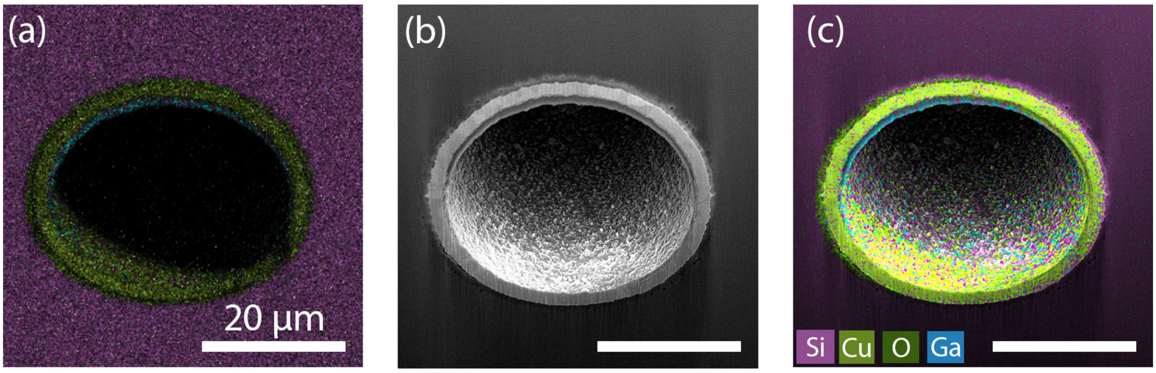

Figure 5.5: IHS image fusion on one of the FIB-SEM(EDS) tomography slices of the sample 9. (a) EDS mapping of overlaid elements, (b) SE image, (c) fused image. Graphic scale is 20 µm.

5.2.2 Pyramid based fusion

This section introduces the concept of pyramid-based fusion method. The principle is in the extraction of high-frequency information from high resolution images and adding it to the lower-resolution images. The input SE image is convoluted with a predefined filter (generally low-pass and bandpass filters) and divided into a number of images with different scales, typically by a factor of two. Via subtraction and subsampling of an input image arises a pyramid-like set of Gaussian and Laplacian images [68], [76], hence the name *Laplacian pyramid fusion method.*

As we are dealing with spectral RGB images, the color space selection is important. During pyramid merging, the IHS model from the previous method was replaced with not so different *Hue-Saturation-Brightness* (HSB) color space [74]. The brightness component, corresponding to pixel values $0 - 255$ from black to the respective saturated color defined by hue, is not tending to suffer from color distortion as intensity due to the double bandwidth size, as the intensity values vary between $0 - 127$ to fully saturated color.

At first (see Figure 5.6), the Laplacian image level 1 is compiled by the subtraction of the input image from its smoothed version to store high frequency information. Let $f(x,y)$ be the original high resolution image, and $G_1(x,y)$ be the Gaussian image result of applying an appropriate low-pass filter to $f(x,y)$ [77]. The Laplacian image of level 1 is given by [78]

$$L_1(x,y) = f(x,y) - G_1(x,y). \tag{5.4}$$

Secondly, the dimension of Gaussian image 1 is reduced by a factor of 2, while the field of view stays the same, thus reducing the number of pixels and as a result halving

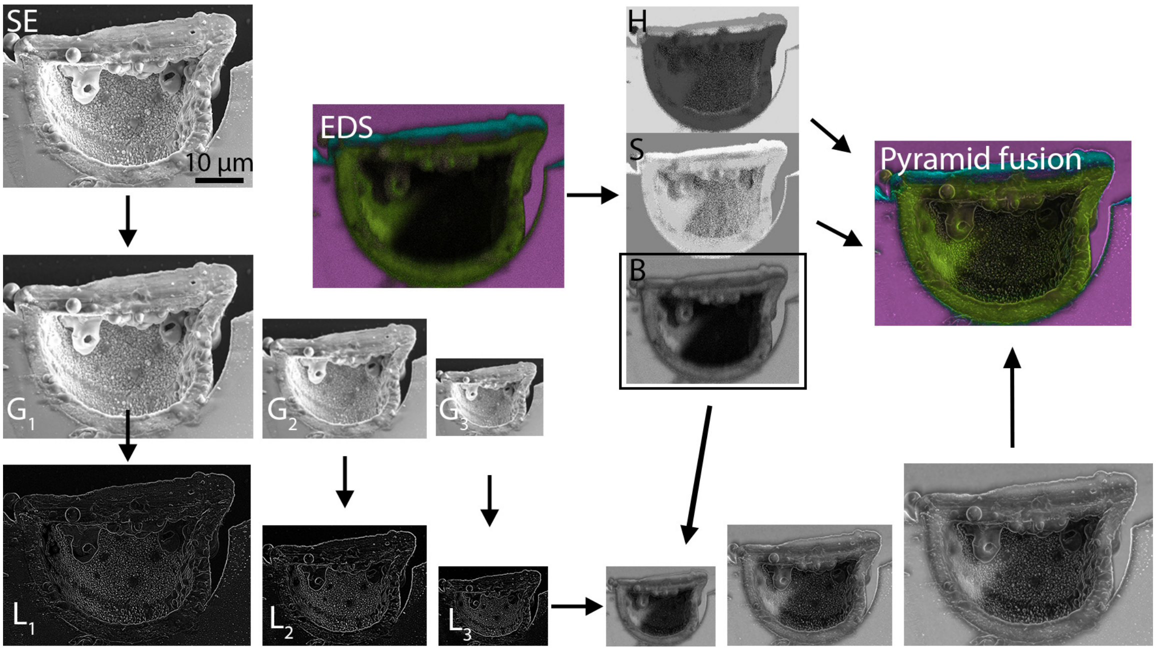

Figure 5.6: Laplacian pyramid fusion concept presented on the sample 9 cross-section and EDS mapping. High resolution SE image is decomposed to the Laplacian pyramid (L_1-L_3). Low-resolution EDS image is divided into color channels by HSB model. Brightness component is introduced to the algorithm and add to the corresponding Laplacian image (L_3). After constructing the new pyramid, the sharpened version is the new brightness channel. Fused image is created after the RGB transformation.

the maximum frequency. Corresponding Laplacian image 2 contains lower frequencies than in 1. In general, with the increasing pyramid level, the filter is concentrated on the lower and mid-spatial frequencies [78]. This iteration continues until the residual image is the same pixel array size as the low resolution spectral matrix and the targeted number of frequency bandwidths is extracted.

Now the to-be-sharpened low resolution image is introduced into the algorithm. The image is divided into color parts according to the HSB model. The brightness component is now added to the corresponding Laplacian image of the same size, upsampled by filling in columns and rows of zeroes, and then blurred by the same sigma Gaussian filter value as during the pyramid built. Image blurring used here is called Gaussian blur and is essentially a transformation centered on each pixel by Gaussian function. This new version is added to the same-sized Laplacian image until all images are processed. The last sharpened version is introduced as the new brightness component and after color merge and RGB transformation, the output represents a highlighted colorful image providing a better possibility of localization and identification whilst keeping the spectral information [74].

After getting a comprehended overview of the technique, a macro was developed in the ImageJ Macro programming language (IJM). This script supports the automation of any two prealigned images in Fiji ImageJ. After its upload, it is necessary to only change the number of desired pyramid steps and a size of the Gaussian filter. The macro will then process the given images using ImageJ commands and plugins according to the step-by-step method described in Figure 5.6.

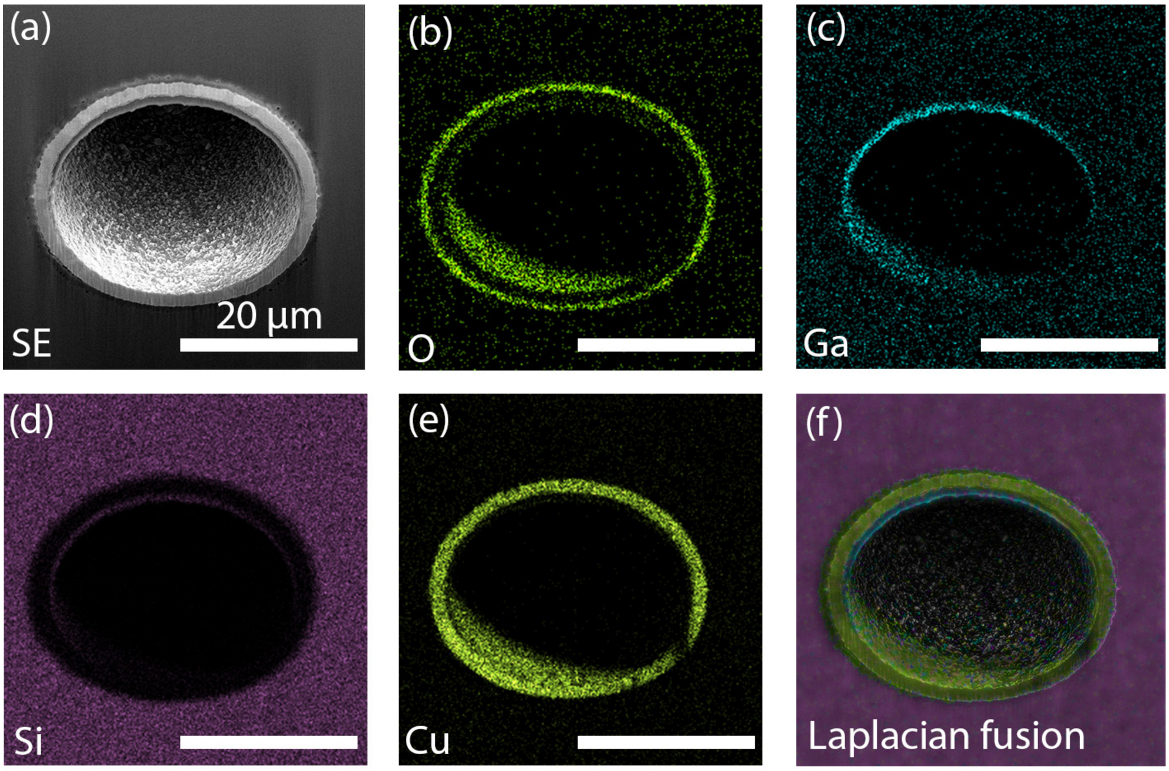

Figure 5.7: LPF example of SE image of the sample 9 tomography cross-section with individual EDS spectral maps. (a) SE, (b) O, (c) Ga, (d) Si, (e) Cu, (f) all images above combined. In comparison to IHS, LPF better keeps the color information. Graphic scale on cross-section images is 20 µm.

Naturally, once a fusion is performed, it is important to interpret and evaluate the images. There are quantitative methods for comparing the accuracy of merged images, but they are beyond the scope of this thesis. And therefore, our discussions were limited to the quality of image correlation, in the sense of registering them to each other before the color fusion, and to the facilitation of human interpretation with respect to the aim of fusion.

CONCLUSION

The presented master's thesis emphasizes the correlative 2D and 3D approach during defect identification of structures from the semiconductor industry. To achieve multimodal material investigation, the methods need to be effectively linked together as no technique can provide all the essential explanations. To demonstrate the capabilities of each instrumentation, test structures of through-silicon-via were elected. During CMOS die fabrication, TSV exhibits a failure rate in the form of leakage current.

Correlative tomography workflow has been successfully set out to target the regions of interest and build up the multi-scale analysis procedure. Selected techniques of XCT, FIB-SEM (EDS), FIB-SIMS, and AFM are outlined and implemented in the correlative approach. Each technique includes a different aspect of correlation and provides distinct insides of the sample. It has been proven how datasets can be effectively used in conjunction with X-ray CT imaging in a correlative manner.

Medium and high resolution XCT introduced the sample as such and located potentially critical defects. Subsequent data processing resolved in 3D object rendering to visualise the faulty areas of TSV and to simulate further FIB approach. Following cross-section topography and chemical composition investigation revealed the possible reasons and origin of the TSV failure in the form of voids, imperfect inner layer deposition, and improper cleaning methods during manufacturing. To facilitate the data interpretation, intensity-hue-saturation and Laplacian pyramid image fusion methods were introduced and implemented with a macro. Furthermore, to understand the trends in impurities as a function of depth, the FIB slice-and-view tomography has been performed with SEM (EDS) and SIMS detection. Careful 3D co-registration of the same volume of interest was then carried out to merge the datasets of non-destructive XCT and destructive FIB tomography.

Further work will aim at improving the accuracy of TOF-SIMS sample holder rotation and its incorporation within the automated script. Additionally, correlative tomography of higher-resolution techniques, i.e., atom probe tomography (APT) [79] or TEM/STEM tomography [80] can be included in the workflow depending on the manufacturer demands and sample specifications.

Overall, the study strengthens the idea of a correlative approach and adds to the growing body of research an additional 3D tomography registration of the underlying bulk by various methods. In conclusion, this thesis fulfils its primary goals and moreover, part of the work was focused on improving FIB milling artifacts and in addition, data visualization in the form of image fusion has been performed.

...And that's all I have to say about that. [Forest Gump, Washington DC, 1994].

REFERENCES

[1] Sjollema, K. A.; Schnell, U.; Kuipers, J.; et al.: Correlated Light Microscopy and Electron Microscopy. In *Correlative Light and Electron MIcroscopy*, ed. by T. Müller-Reichert; P. Verkade, Academic Press, 2012, ISBN 9780124160262, p. 157–173, doi:10.1016/B978-0-12-416026-2.00009-1.

[2] Carmignato, S.; Dewulf, W.; Leach, R.: *Industrial X-ray computed tomography*. Cham: Springer International Publishing, 2018, ISBN 978-3-319-59573-3, 369 p., doi:10.1007/978-3-319-59573-3.

[3] ZEISS: *Correlative Microscopy Materials Sciences*. Chichester, UK: John Wiley & Sons, nov 2017, ISSN 2038-8306, 34 p.

[4] Begemann, I.; Galic, M.: Correlative Light Electron Microscopy: Connecting Synaptic Structure and Function. *Frontiers in Synaptic Neuroscience*, vol. 8, aug 2016: p. 1–12, ISSN 1663-3563, doi:10.3389/fnsyn.2016.00028.

[5] Burnett, T. L.; McDonald, S. A.; Gholinia, A.; et al.: Correlative Tomography. *Scientific Reports*, vol. 4, 1, may 2015: p. 4711, ISSN 2045-2322, doi:10.1038/srep04711.

[6] Utke, I.; Moshkalev, S.; Russell, P. (editors): *Nanofabrication Using Focused Ion and Electron Beams: Principles and Applications*. New Yor: Oxford University Press, 2012, ISBN 978-0-19-973421-4, 813 p.

[7] Burnett, T.; Kelley, R.; Winiarski, B.; et al.: Large volume serial section tomography by Xe Plasma FIB dual beam microscopy. *Ultramicroscopy*, vol. 161, feb 2016: p. 119–129, ISSN 03043991, doi:10.1016/j.ultramic.2015.11.001.

[8] Baruchel, J.; Buffière, J.-Y.; Maire, E.; et al.: *X-Ray Tomography in Material Science*. Paris: HERMES Science Publications, 2000, ISBN 9781118480489.

[9] Liu, Y.; King, H.; van Huis, M.; et al.: Nano-Tomography of Porous Geological Materials Using Focused Ion Beam-Scanning Electron Microscopy. *Minerals*, vol. 6, 4, oct 2016: p. 104, ISSN 2075-163X, doi:10.3390/min6040104.

[10] Nan, N.; Wang, J.: FIB-SEM Three-Dimensional Tomography for Characterization of Carbon-Based Materials. *Advances in Materials Science and Engineering*, vol. 2019, 1, 2019: p. 1–8, ISSN 1687-8434, doi:10.1155/2019/8680715.

[11] Vařeka, K.: *2D a 3D analýza polovodičových struktur metodou SIMS*. Bachelor's thesis, 50 p., University of Technology, Faculty of Mechanical Engineering. Supervisor Ing. Petr Bábor, Ph.D., 2019.

[12] Schindelin, J.; Arganda-Carreras, I.; Frise, E.; et al.: Fiji: an open-source platform for biological-image analysis. *Nature Methods*, vol. 9, 7, jul 2012: p. 676–682, ISSN 1548-7091, doi:10.1038/nmeth.2019.

[13] Carl ZEISS X-Ray Microscopy Inc.: Xradia XMReconstructor.

[14] Stock, S. R.: *MicroComputed Tomography: Methology and applications*. NW: CRC Press, 1. ed., dec 2008, ISBN 9780429186745, 349 p., doi:10.1201/9780429186745.

[15] Van Der Heide, P.: *Secondary Ion Mass Spectrometry: An Introduction to Principles and Practices*. Hoboken, New Jersey: John Wiley & Sons, Inc., aug 2014, ISBN 978-1-118-48048-9, 365 p.

[16] Šamořil, T.: *Aplikace fokusovaného iontového a elektronového svazku v nanotechnologiích*. Dissertation thesis, 126 p., Brno University of Technology, Faculty of Mechanical Engineering. Supervisor Prof. RNDr. Tomáš Šikola, CSc., 2015.

[17] Nan, Y. (editor): *Focused Ion Beam Systems*, vol. 9780521831. Cambridge: Cambridge University Press, 2007, ISBN 9780511600302, 1–391 p., doi:10.1017/CBO9780511600302.

[18] Orloff, J.; Utlaut, M.; Swanson, L.: *High Resolution Focused Ion Beams: FIB and its Applications*. Boston, MA: Springer US, 2003, ISBN 978-1-4613-5229-7, 303 p., doi:10.1007/978-1-4615-0765-9.

[19] Cui, Z.: *Nanofabrication: Principles, Capabilities and*. Boston, MA: Springer US, 2008, ISBN 978-1-4419-4536-5, 343 p., doi:10.1007/978-0-387-75577-9.

[20] Forbes, R. G.: Field evaporation theory: a review of basic ideas. *Applied Surface Science*, vol. 87-88, C, mar 1995: p. 1–11, ISSN 01694332, doi:10.1016/0169-4332(94)00526-5.

[21] Orloff, J. (editor): *Handbook of Charged Particle Optics*. Boca Raton: CRC Press/Taylor & Francis, 2. ed., 2009, ISBN 978-1-4200-4554-3, 688 p.

[22] Forbes, R. G.: Understanding how the liquid-metal ion source works. *Vacuum*, vol. 48, 1, 1997: p. 85–97, ISSN 0042207X, doi:10.1016/s0042-207x(96)00227-8.

[23] Kingham, D. R.; Swanson, L. W.: Theoretical investigation of liquid metal ion sources: Field and temperature dependence of ion emission. *Applied Physics A Solids and Surfaces*, vol. 41, 2, 1986: p. 157–169, ISSN 07217250, doi:10.1007/BF00631124.

[24] What is FIB - Orsay Physics. 2021, Accessed 2021-02-24.
URL <`https://www.orsayphysics.com/what-is-fib`>

[25] Gierak, J.: Focused ion beam technology and ultimate applications. *Semiconductor Science and Technology*, vol. 24, 4, apr 2009: p. 043001, ISSN 0268-1242, doi:10.1088/0268-1242/24/4/043001.

[26] Jamaludin, F. S.; Mohd Sabri, M. F.; Said, S. M.: Controlling parameters of focused ion beam (FIB) on high aspect ratio micro holes milling. *Microsystem Technologies*, vol. 19, 12, dec 2013: p. 1873–1888, ISSN 0946-7076, doi:10.1007/s00542-013-1912-y.

[27] Reuteler, J.: FIB artifacts and how to overcome them. In *EuFN FIB workshop*, Graz, 2017, p. 1–25.

[28] Vanden Eynde, X.: *Polymer surfaces studied by ToF-SIMS (Time-of-Flight Secondary Ion Mass Spectrometry) Molecular weight effects and quantification*. Dissertation thesis, Université catholique de Louvain, 1999, doi:10.13140/RG.2.2.15987.63520.

[29] Ziegler, J. F.; Biersack, J. P.; Ziegler, M. D.: *SRIM: The Stopping and Range of Ions in Matter*. Maryland: SRIM Co., 2008, ISBN 978-0-9654207-1-6, 398 p.

[30] Evans Analytical Group: SIMS Theory Tutorial. 2009, Accessed 2021-04-10.
URL <`https://www.eag.com/resources/tutorials/sims-tutorial-theory/`>

[31] Alford, T. L.; Feldman, L. C.; Mayer, J. W.: *Fundamentals of Nanoscale Film Analysis*. Boston, MA: Springer US, 2007, ISBN 978-0-387-29260-1, 337 p., doi:10.1007/978-0-387-29261-8.

[32] Ziegler, J. F.; Biersack, J. P.; Ziegler, M. D.: SRIM Tutorial # 2 – Target Mixing and Sputtering. 2008.

[33] Zalm, P.: Secondary ion mass spectrometry. *Vacuum*, vol. 45, 6-7, jun 1994: p. 753–772, ISSN 0042207X, doi:10.1016/0042-207X(94)90113-9.

[34] Sigmund, P.: Sputtering by ion bombardment: Theoretical concepts. In *Sputtering by ion bombardment I: Physical Sputtering of Single-Element Solids*, ed. by R. Behrisch, Springer Berlin Heidelberg, 1981, ISBN 978-3-540-10521-3, p. 9–71, doi:10.1007/3540105212_7.

[35] Priebe, A.; Xie, T.; Bürki, G.; et al.: The matrix effect in TOF-SIMS analysis of two-element inorganic thin films. *Journal of Analytical Atomic Spectrometry*, vol. 35, 6, 2020: p. 1156–1166, ISSN 0267-9477, doi:10.1039/C9JA00428A.

[36] Cole, D. A.; Attavar, S.; Zhang, L.: Surface Analysis Methods for Contaminant Identification. In *Developments in Surface Contamination and Cleaning*, vol. 1, Elsevier, 2. ed., 2016, ISBN 9780323299602, p. 333–394, doi:10.1016/B978-0-323-29960-2.00008-3.

[37] Krivanek, O.: 2020 Kavli Prize Winners – NANOSCIENCE: Harald Rose and Ondrej Krivanek. 2020, Accessed 2021-04-15.
URL <`https://www.youtube.com/watch?v=p9z4QvoUzGs&list=PLGfr88T8l0jznU0aom8IyJBYS6mprgUs0&index=5`>

[38] Reimer, L.: *Scanning Electron Microscopy: Physics of Image Formation and Microanalysis*, *Springer Series in Optical Sciences*, vol. 45. Berlin, Heidelberg: Springer

Berlin Heidelberg, 2. ed., 1998, ISBN 978-3-642-08372-3, 529 p., doi:10.1007/978-3-540-38967-5.

[39] Goldstein, J. I.; Newbury, D. E.; Michael, J. R.; et al.: *Scanning Electron Microscopy and X-ray Microanalysis*. New York, NY: Springer New York, 2017, ISBN 9781493966769, 1–550 p., doi:10.1007/978-1-4939-6676-9.

[40] Nanakoudis, A.: SEM: Types of Electrons and the Information They Provide. 2019, Accessed 2021-04-18.
URL <`https://www.thermofisher.com/blog/microscopy/sem-signal-types-electrons-and-the-information-they-provide/`>

[41] Burdet, P.: *Three Dimensional Microanalysis by Energy Dispersive Spectrometry: Improved data processing*. Dissertation thesis, École Polytechnique, 2012, doi:10.5075/epfl-thesis-5501.

[42] Scimeca, M.; Bischetti, S.; Lamsira, H. K.; et al.: Energy Dispersive X-ray (EDX) microanalysis: A powerful tool in biomedical research and diagnosis. *European Journal of Histochemistry*, vol. 62, 1, mar 2018: p. 89–99, ISSN 2038-8306, doi:10.4081/ejh.2018.2841.

[43] Bruker-Nano: Introduction to EDS analysis: Reference Manual. 2011.
URL <`http://emc.missouri.edu/wp-content/uploads/2016/01/Bruker-Introduction-to-EDS-analysis.pdf`>

[44] Shen, W.-W.; Chen, K.-N.: Three-Dimensional Integrated Circuit (3D IC) Key Technology: Through-Silicon Via (TSV). *Nanoscale Research Letters*, vol. 12, 1, dec 2017: p. 56, ISSN 1931-7573, doi:10.1186/s11671-017-1831-4.

[45] Gambino, J. P.; Adderly, S. A.; Knickerbocker, J. U.: An overview of through-silicon-via technology and manufacturing challenges. *Microelectronic Engineering*, vol. 135, January, mar 2015: p. 73–106, ISSN 01679317, doi:10.1016/j.mee.2014.10.019.

[46] Motoyoshi, M.: Through-Silicon Via (TSV). *Proceedings of the IEEE*, vol. 97, 1, jan 2009: p. 43–48, ISSN 00189219, doi:10.1109/JPROC.2008.2007462.

[47] Ramm, P.; Wolf, M. J.; Klumpp, A.; et al.: Through Silicon Via Technology - Processes and Reliability for Wafer-Level 3D System Integration. In *2008 58th Electronic Components and Technology Conference*, Lake Buena Vista, FL, USA, jun 2008, p. 841–846, doi:10.1109/ECTC.2008.4550074.

[48] Baliga, B. J.: *Fundamentals of Power Semiconductor Devices*. Boston, MA: Springer US, 2008, ISBN 978-0-387-47313-0, doi:10.1007/978-0-387-47314-7.

[49] Gambino, J. P.; Bowe, W.; Bronson, D. M.; et al.: Imaging of through-silicon vias using X-Ray computed tomography. In *Proceedings of the 21th International Symposium on the Physical and Failure Analysis of Integrated Circuits (IPFA)*, 802, IEEE, jun 2014, ISBN 978-1-4799-3929-9, p. 327–331, doi:10.1109/IPFA.2014.6898170.

[50] Sekhar, V. N.; Sam Neo; Li Hong Yu; et al.: Non-destructive testing of a high dense small dimension through silicon via (TSV) array structures by using 3D X-ray computed tomography method (CT scan). In *2010 12th Electronics Packaging Technology Conference*, IEEE, dec 2010, ISBN 978-1-4244-8560-4, p. 462–466, doi:10.1109/EPTC.2010.5702683.

[51] Agulleiro, J.-I.; Fernandez, J.-J.: Tomo3D 2.0 – Exploitation of Advanced Vector eXtensions (AVX) for 3D reconstruction. *Journal of Structural Biology*, vol. 189, 2, feb 2015: p. 147–152, ISSN 10478477, doi:10.1016/j.jsb.2014.11.009.

[52] FEI SAS: Avizo 8: User´s Guide. 2014.

[53] Bankhead, P.: Analyzing fluorescence microscopy images with ImageJ. Technical report, Queen´s University Belfast, may 2014.

[54] WEST, G.; THOMSON, R.: Combined EBSD/EDS tomography in a dual-beam FIB/FEG-SEM. *Journal of Microscopy*, vol. 233, 3, mar 2009: p. 442–450, ISSN 00222720, doi:10.1111/j.1365-2818.2009.03138.x.

[55] Cantoni, M.; Burdet, P.: Microanalysis in a FIB/SEM: EDX in 3D. In *What can we expect, where are the limits*, Graz, Centre Interdisciplinaire de Microscopie Electronique: École Polytechnique Fédérale de Lausanne, 2017, p. 19.
URL <`https://www.eu-f-n.org/cms/wp-content/uploads/2017/07/eu-f-n_2017-3d-edx-tutorial.pdf`>

[56] Šikula, M.; Hrnčíř, T.; Gounet, P.: Rapid cross-sectioning of challenging samples using a combination of TRUE X-sectioning and the rocking stage techniques. In *24th International Symposium on the Physical and Failure Analysis of Integrated Circuits (IPFA)*, July 2017, p. 1–3, doi:10.1109/IPFA.2017.8060168.

[57] Binnig, G.; Quate, C. F.; Gerber, C.: Atomic Force Microscope. *Physical Review Letters*, vol. 56, 9, mar 1986: p. 930–933, ISSN 0031-9007, doi:10.1103/PhysRevLett.56.930.

[58] Mironov, V.: *Fundamentals of Scanning Probe Microscopy*. The Russian Academy of Sciences, 2004, 97 p.

[59] McPhail, D. S.; Chater, R. J.; Li, L.: Applications of focused ion beam SIMS in materials science. *Microchimica Acta*, vol. 161, 3-4, jun 2008: p. 387–397, ISSN 0026-3672, doi:10.1007/s00604-007-0913-x.

[60] Barnes, J.-P.; Djomeni, L.; Minoret, S.; et al.: Focused ion beam time-of-flight secondary ion mass spectroscopy tomography of through-silicon vias for 3D integration. *Journal of Vacuum Science & Technology B*, vol. 34, 3, may 2016: p. 03H137, ISSN 2166-2746, doi:10.1116/1.4947463.

[61] Mičulka, M.: *Tomografická analýza polovidčových struktur metodou FIB-SIMS*. Bachelor's thesis, 47 p., Brno University of Technology, Faculty of Mechanical Engineering, Supervisor Ing. Petr Bábor, Ph.D., 2020.

[62] Karlovský, J.: *Příprava řezů vzorků a jejich analýza metodou SIMS*. Master's thesis, 62 p., Brno University of Technology, Faculty of Mechanical Engineering, Supervisor Ing. Petr Bábor, Ph.D., 2018.

[63] SmarAct: SLC-1720 - Linear Piezo Stage. 2021, Accessed 2021-05-09.
URL `<https://www.smaract.com/linear-stages/product/slc-1730>`

[64] Gonzalez, R. C.; Woods, R. E.: *Digital Image Processing*. Upper Saddle River: Pearson Education, Inc., 3. ed., 2008, ISBN 978-0-13-168728-8, 977 p.

[65] Eisaku, O.: Digital Image Processing Technology for Scanning Electron Microscopy. In *Advances in imaging and electron physics*, vol. 105, Tokyo: Academic Press, 1999, ISBN 0-12-014747-5, p. 78–137.

[66] LIU, S.; SUN, L.; GAO, J.; et al.: A fast curtain-removal method for 3D FIB-SEM images of heterogeneous minerals. *Journal of Microscopy*, vol. 272, 1, oct 2018: p. 3–11, ISSN 00222720, doi:10.1111/jmi.12723.

[67] TESCAN Rocking Stage | TESCAN. 2021, Accessed 2021-02-25.
URL `<https://www.tescan.com/product/tescan-rocking-stage/>`

[68] Mishra, D.; Palkar, B.: Image Fusion Techniques: A Review. *International Journal of Computer Applications*, vol. 130, 9, 2015: p. 7–13, doi:10.5120/ijca2015907084.

[69] Cardona, A.; Saalfeld, S.; Schindelin, J.; et al.: TrakEM2 Software for Neural Circuit Reconstruction. *PLoS ONE*, vol. 7, 6, jun 2012: p. e38011, ISSN 1932-6203, doi:10.1371/journal.pone.0038011.

[70] Thevenaz, P.; Ruttimann, U.; Unser, M.: A pyramid approach to subpixel registration based on intensity. *IEEE Transactions on Image Processing*, vol. 7, 1, jan 1998: p. 27–41, ISSN 10577149, doi:10.1109/83.650848.

[71] Bulgarelli, J.; Tazzari, M.; Granato, A. M.; et al.: Dendritic Cell Vaccination in Metastatic Melanoma Turns "Non-T Cell Inflamed" Into "T-Cell Inflamed" Tumors. *Frontiers in Immunology*, vol. 10, oct 2019: p. 2353, ISSN 1664-3224, doi:10.3389/fimmu.2019.02353.

[72] Lowe, D. G.: Distinctive Image Features from Scale-Invariant Keypoints. *International Journal of Computer Vision*, vol. 60, 2, nov 2004: p. 91–110, ISSN 0920-5691, doi:10.1023/B:VISI.0000029664.99615.94.

[73] Arganda-Carreras, I.; Sorzano, C. O. S.; Marabini, R.; et al.: Consistent and Elastic Registration of Histological Sections Using Vector-Spline Regularization. In *Computer Vision Approaches to Medical Image Analysis*, Springer Berlin Heidelberg, 2006, p. 85–95, doi:10.1007/11889762_8.

[74] Vollnhals, F.; Audinot, J.-N.; Wirtz, T.: Correlative Microscopy Combining Secondary Ion Mass Spectrometry and Electron Microscopy: Comparison of Intensity–Hue–Saturation and Laplacian Pyramid Methods for Image Fusion. *Analytical Chemistry*, vol. 89, 20, oct 2017: p. 10702–10710, ISSN 0003-2700, doi:10.1021/acs.analchem.7b01256.

[75] Harris, J. R.; Murray, R.; Hirose, T.: IHS transform for the integration of radar imagery with other remotely sensed data. *Photogrammetric Engineering & Remote Sensing*, vol. 56, 12, 1990: p. 1631–1641, ISSN 0099-1112.

[76] Kumari, S.; Malviya, M.; Lade, S.: Image Fusion techniques based on pyramid decomposition. *International Journal of Artificial Intelligence and Mechatronics*, vol. 2, 4, 2014: p. 127–130, ISSN 2320-5121.

[77] Sadjadi, F.: Comparative Image Fusion Analysais. In *2005 IEEE Computer Society Conference on Computer Vision and Pattern Recognition (CVPR'05) - Workshops*, vol. 3, IEEE, 2006, ISBN 0-7695-2372-2, p. 8–8, doi:10.1109/CVPR.2005.436.

[78] Burt, P.; Adelson, E.: The Laplacian Pyramid as a Compact Image Code. *IEEE Transactions on Communications*, vol. 31, 4, apr 1983: p. 532–540, ISSN 0096-2244, doi:10.1109/TCOM.1983.1095851.

[79] Rickard, W. D.; Reddy, S. M.; Saxey, D. W.; et al.: Novel Applications of FIB-SEM-Based ToF-SIMS in Atom Probe Tomography Workflows. *Microscopy and Microanalysis*, vol. 26, 4, aug 2020: p. 750–757, ISSN 1431-9276, doi:10.1017/S1431927620000136.

[80] LI, M.-h.; YANG, Y.-q.; HUANG, B.; et al.: Development of advanced electron tomography in materials science based on TEM and STEM. *Transactions of Nonferrous Metals Society of China*, vol. 24, 10, oct 2014: p. 3031–3050, ISSN 10036326, doi:10.1016/S1003-6326(14)63441-5.

LIST OF ABBREVIATIONS

CM	Correlative Microscopy
CLEM	Correlative Light Electron Microscopy
1D	One-dimensional
2D	Two-dimensional
3D	Three-dimensional
FIB	Focused Ion Beam
SIMS	Secondary Ion Mass Spectrometry
SEM	Scanning Electron Microscopy
EDS	Energy-Dispersive Spectroscopy
XCT	X-ray Computed Tomography
AFM	Atomic Force Microscopy
CMOS	Complementary Metal Oxide Semiconductor
TSV	Through-Silicon-Via
IC	Integrated Circuit
ROI	Region Of Interest
VOI	Volume Of Interest
EBSD	Electron Backscatter Diffraction
SI	Secondary Ions
TOF	Time-Of-Flight
LMIS	Liquid Metal Ion Source
FEV	Field Evaporation
FIBID	Focused Ion Beam Induced Deposition
TEM	Transmission Electron Microscope

STEM	Scanning Transmission Electron Microscope
EDS	Energy-Dispersive X-ray Spectroscopy
CL	Cathodoluminescence
PE	Primary Electron
SE	Secondary Electron
BSE	Backscattered Electron
AE	Auger Electron
SDD	Silicon Drift Detector
ADC	Analog-to-Digital Converter
CCD	Charge-Coupled Device
FEOL	Front-End-Of-Line
BEOL	Back-End-Of-Line
CVD	Chemical Vapor Deposition
PVD	Physical Vapor Deposition
RIE	Reactive-Ion Etching
GIS	Gas Injection System
ETD	Everhart-Thornley Detector
SPM	Scanning Probe Microscopy
CPEM	Correlative Probe Electron Microscopy
UHV	Ultra High Vacuum
IHS	Intensity-Hue-Saturation color space
HSB	Hue-Saturation-Brightness color space
BUT	Brno University of Technology
LPF	Laplacian Pyramid Fusion
IJM	ImageJ Macro language